



NTNU – Trondheim
Norwegian University of
Science and Technology

Models and numerical methods for two-phase flow of CO₂ in pipes

Aleksander Reinertsen

Master of Science in Mechanical Engineering

Submission date: June 2015

Supervisor: Bernhard Müller, EPT

Co-supervisor: Svend Tollak Munkejord, Sintef
Morten Hammer, Sintef

Norwegian University of Science and Technology
Department of Energy and Process Engineering

EPT-M-2015-69

MASTER THESIS

for

Student Aleksander Reinertsen

Spring 2015

Models and numerical methods for two-phase flow of CO₂ in pipes*Modeller og numeriske metoder for tofasestrømning av CO₂ i rør***Background and objective**

Carbon dioxide (CO₂) is a greenhouse gas produced in numerous industrial processes. One way to reduce the global warming is to separate the CO₂ from the processes and to inject it into a geological formation. This will most often involve pipe transport. Should a crack arise in the pipe, a running fracture might form, depending on the pressure-propagation velocity in the fluid. Furthermore, the CO₂ in the pipe will not be pure, and this will influence its thermophysical properties.

In the BIGCCS Centre, SINTEF is developing a coupled fluid-structure model aimed at developing a better understanding of how to avoid running fractures in a cost-effective way. An important part of the model is the development of an accurate and efficient method to simulate the thermo and fluid part, which involves single- and two-phase flow. The present project will consider the AUSM method.

The student's project from last autumn will form a starting point for the work. In addition, a library providing routines for real CO₂ thermodynamics will be provided by SINTEF.

The following tasks are to be considered:

1. Get familiar with the use of the thermodynamics library.
2. Implement AUSM schemes for two-phase flow models. In particular, this includes the implementation of routines to calculate the primitive variables from the conserved variables.
3. The work will be performed in a step-wise fashion, starting with the Euler equations and proceeding with the homogeneous equilibrium model (HEM).
4. The resulting numerical models should be analysed and tested with respect to accuracy and robustness, employing suitable test cases.
5. If possible, comparison with alternative numerical schemes should be carried out.
6. The work will be documented in a technical report.

-- " --

Within 14 days of receiving the written text on the master thesis, the candidate shall submit a research plan for his project to the department.

When the thesis is evaluated, emphasis is put on processing of the results, and that they are presented in tabular and/or graphic form in a clear manner, and that they are analyzed carefully.

The thesis should be formulated as a research report with summary both in English and Norwegian, conclusion, literature references, table of contents etc. During the preparation of the text, the candidate should make an effort to produce a well-structured and easily readable report. In order to ease the evaluation of the thesis, it is important that the cross-references are correct. In the making of the report, strong emphasis should be placed on both a thorough discussion of the results and an orderly presentation.

The candidate is requested to initiate and keep close contact with his/her academic supervisor(s) throughout the working period. The candidate must follow the rules and regulations of NTNU as well as passive directions given by the Department of Energy and Process Engineering.

Risk assessment of the candidate's work shall be carried out according to the department's procedures. The risk assessment must be documented and included as part of the final report. Events related to the candidate's work adversely affecting the health, safety or security, must be documented and included as part of the final report. If the documentation on risk assessment represents a large number of pages, the full version is to be submitted electronically to the supervisor and an excerpt is included in the report.

Pursuant to "Regulations concerning the supplementary provisions to the technology study program/Master of Science" at NTNU §20, the Department reserves the permission to utilize all the results and data for teaching and research purposes as well as in future publications.

The final report is to be submitted digitally in DAIM. An executive summary of the thesis including title, student's name, supervisor's name, year, department name, and NTNU's logo and name, shall be submitted to the department as a separate pdf file. Based on an agreement with the supervisor, the final report and other material and documents may be given to the supervisor in digital format.

- Work to be done in lab (Water power lab, Fluids engineering lab, Thermal engineering lab)
 Field work

Department of Energy and Process Engineering, 14. January 2015



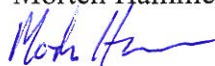
Olav Bolland
Department Head



Bernhard Müller
Academic Supervisor



Research Advisors: Svend Tollak Munkejord, SINTEF Energy Research
Morten Hammer, SINTEF Energy Research



Abstract

Key to the transport phase of carbon capture and storage (CCS) is understanding the behavior of liquid or supercritical CO_2 in pipelines, and the consequences of cracks and pipe depressurization. It is therefore useful to develop mathematical models and numerical methods for two-phase flow of CO_2 in pipes in order to better predict such behavior. Such developed tools can also be useful in fluid structure-interaction models.

Key to simulating single or multiphase flows is the formulation of a flow model. Here, the homogeneous equilibrium model (HEM) has been used. Further, for a flow model such as HEM, closure conditions are needed, and in this thesis the Span-Wagner equation of state (EOS) has been used. This EOS is a Helmholtz function fitted to experimental data for CO_2 properties, and so it is CO_2 -specific.

When using the finite volume method to simulate fluid flow, a numerical flux function is needed. In this thesis, the advection upstream splitting method (AUSM) family of schemes has been investigated and compared to the first ordered centered (FORCE) scheme in order to evaluate the performance of AUSM-schemes.

AUSM⁺-up has been found to perform satisfactorily for three test cases. Due to the upstream nature of the scheme, it proved more accurate than the FORCE and Lax-Friedrichs schemes for a test case simulating the advection of a CO_2 gas fraction in liquid. When compared to the results obtained by SINTEF Energy Research for a shock tube case and a depressurization case, AUSM⁺-up was found to reproduce all the expected solution features seen for the FORCE solution. For the shock tube case, slight differences in the evaluation of energy, temperature and velocity could be seen. Possible reasons for this could be that the solution is not grid-independent or that the flux splitting nature of AUSM schemes simply causes these variables to be evaluated slightly differently, possibly more accurately, compared to FORCE.

When simulating the shock tube and the depressurization cases, the thermodynamic solver had problems evaluating the speed of sound correctly. This did not seem to affect the solution of state variables to a large degree. These problems occurred in regions where the thermodynamic solver evaluated certain cells to be liquid phase, whereas other cells were liquid with a fractional amount of gas. Such problems were not seen for FORCE and this is a drawback for AUSM⁺-up.

A further drawback for AUSM⁺-up is that it requires parameter tuning, and the solution of the shock tube test case was parameter sensitive in order to obtain the correct solution. Another finding when comparing AUSM⁺-up and FORCE for the depressurization case was that the former has higher computational times for equal grid sizes. This increased computational cost is however well paid off by its better resolution compared with the FORCE scheme.

The implementation of AUSM schemes proved complicated due to the need for parameter tuning, but the scheme performed satisfactorily for all test cases. The implementation of FORCE was comparably straightforward. Thus it could be worth investigating AUSM schemes that do not require parameter-tuning. Future work could also include implementing other flow models where one would avoid regions of oscillating speed of sound. Optimization of the AUSM⁺-up code is also a possible future task.

Sammendrag

En viktig brikke i transportfasen av karbonfangst og -lagring (CCS) er forståelsen av hvordan flytende eller superkritisk CO₂ oppfører seg i rør, samt forståelsen av konsekvensene av sprekker eller trykkavlastning i røret. Av denne grunn er det nyttig å utvikle matematiske modeller og numeriske metoder for tofasestrømning av CO₂ i rør, for bedre å kunne forutsi oppførselen i seg selv og for å kunne bruke disse numeriske verktøyene i fluid-struktur interaksjonsmodeller.

Videre er det nødvendig å formulere en strømningsmodell for å simulere enfase- eller tofasestrømning. I denne oppgaven har homogen likevektsmodell (HEM) blitt brukt. I tillegg trenger man for en modell som HEM å relatere tilstandsvariabler ved hjelp av en tilstandsligning. I denne oppgaven har Span-Wagner-tilstandsligningen blitt brukt til dette formålet. Span-Wagner-tilstandsligningen er en Helmholtz-funksjon tilpasset eksperimentelle CO₂-data.

Når man bruker endelig volum-metode (engelsk: *finite volume method*) (FVM) for å simulere strømning av et fluid, trenger man en numerisk fluksfunksjon. I denne oppgaven har en familie av metoder kalt *advection upstream splitting method* (AUSM) blitt brukt til dette formålet. I tillegg har metoden blitt sammenlignet med en annen metode kalt *first ordered centered scheme* (FORCE).

AUSM⁺-up lyktes i å simulere tre forskjellige tester. Ettersom denne metoden er en oppstrøms metode, var den mer nøyaktig enn FORCE-metoden og Lax-Friedrichs-metoden for simulering av advektering en CO₂-gassfraksjon i væske. Ved sammenligning av resultater funnet av SINTEF Energi for én shock-tube-test og én trykkavlastningstest, ble AUSM⁺-up funnet å produsere resultater med de samme løsningskarakteristikkene man kunne se for FORCE-løsningen. For shock-tube-testen var det små forskjeller i energi, temperatur og hastighet. Dette kan skyldes at løsningen ikke var grid-uavhengig, eller at fluks-splittingen man ser i AUSM fører til andre, muligens mer nøyaktige resultater.

Ved simuleringen av testene med shock-tube og trykkavlastning hadde den termodynamiske løseren problemer med å regne ut lydfarten på en tilfredsstillende måte. Dette påvirket ikke utregningen av tilstandsvariablene i stor grad. Problemene oppsto i områder der den termodynamiske løseren evaluerte enkelte celler til å være væskefase, mens andre celler ble evaluert til å være væskefase med et lite innhold av gass. Slike problemer oppstod ikke for simuleringer med FORCE.

En videre ulempe med AUSM⁺-up er at metoden krever parameter-tuning. Løsningen av shock-tube-caset var sensitivt til valg av parameterverdier for å oppnå riktig løsning. En videre observasjon gjort ved sammenligning av AUSM⁺-up og FORCE var at førstnevnte hadde høyere kjøretider. Denne ulempen kan imidlertid oppveies av at AUSM⁺-up tilsynelatende har mer nøyaktige resultater.

Implementeringen av AUSM-metoder viste seg å være vanskelig som følge av behovet for parameter-tuning, men metoden ga tilfredsstillende resultater for alle tre testene som ble utført. Implementeringen av FORCE var ukomplisert. Av denne grunn kan det være interessant å videre se på AUSM-metoder som ikke krever parameter-tuning. Videre arbeid kan også være implementeringen av AUSM-skjemaer for andre strømningsmodeller, hvor man ikke opplever oscillerende lydfart. Optimalisering av AUSM⁺-up-koden kan også være mulig videre arbeid.

Preface

As I conclude my five-year integrated Master's degree at NTNU with this thesis, certain names should not go unmentioned. Firstly I would like to thank my supervisors, Morten Hammer, Svend Tollak Munkejord and especially Bernhard Müller for contributing to my final year at NTNU being the most interesting, motivating and encouraging of the four years I spent there.

Secondly I would like to thank all the people who made my time at the University of Minnesota so special. A special thank you to Hyunki Sul and especially Pratik Mukherjee for their impact on my engineering career. Crucial.

Further I would like to thank Berit and Jonny Kristiansen for all their help during my time in Trondheim. Thank you for being unusually kind and patient, for providing me with means of transportation, countless meals and permanent temporary shelter.

And finally, to my mom and dad, Trine and Trond, I want to say thank you for all your love and support that you always have given and continue to give me. I would not have been here without your strength and encouragement. Thank you to my two wonderful sisters, Amalie and Andrea, for being more than just blood relatives, and to the latter also for being a great support throughout our years together in Trondheim.

Aleksander Reinertsen
Aleksander Reinertsen
Trondheim, June 2015

Contents

Abstract	5
Sammendrag	6
Preface	7
List of figures	11
List of tables	12
Nomenclature	13
1 Introduction	17
1.1 Background	17
1.1.1 CO ₂ tranport	18
1.2 Thesis aim and relevance	18
1.3 Thesis outline	19
1.4 Numerical simulation framework	19
1.5 Acknowledgments	19
2 Multiphase flow	21
2.1 Key concepts	21
2.2 Multiphase flow models	21
2.3 Homogeneous equilibrium model	22
2.3.1 Speed of sound	24
3 Numerical methods for fluid dynamics	27
3.1 Finite volume method	27
3.2 Accuracy and stability	29
3.2.1 Determining error, order of accuracy and rate of convergence . . .	29
3.2.2 Increasing the order of accuracy	30
3.2.3 Courant-Friedrichs-Lewy number	31
3.3 MUSCL	31
3.4 Time integration methods	34
3.4.1 Explicit Euler method	35
3.4.2 Heun's method	36
3.4.3 Other time integration methods	36
3.5 AUSM family	36
3.5.1 AUSM ⁺	38
3.5.2 AUSM ⁺ -up	39
3.6 Lax-Friedrichs scheme	42
3.7 FORCE scheme	42

3.8	Boundary conditions	43
4	Thermodynamics	45
4.1	Equation of state	45
4.2	Span-Wagner equation of state	45
4.2.1	Calculating primitive variables	46
4.2.2	Calculating variables from entropy, s , and pressure, p	46
5	Results and discussion	47
5.1	Simple advection in a 12 m tube	47
5.2	Shock tube	54
5.2.1	Speed of sound problems with AUSM schemes	58
5.2.2	Parameter tuning problems with AUSM schemes	60
5.3	Depressurization of pipe	61
6	Conclusions and further work	69
	Bibliography	73

List of Figures

2.1	Speed of sound at evaluated saturation pressure (4.16 MPa) for temperature 280.0 K.	25
3.1	One-dimensional discretization used in calculations. Control volumes around each node, where cell-averages are stored, and locations of the faces, where the numerical fluxes are calculated, indicated.	29
3.2	Illustration of cell average of arbitrary variable in grid.	32
3.3	Illustration of linearly reconstructed cell variables.	33
5.1	Grid refinement of advected Gauss curve in 12 m tube. AUSM ⁺	48
5.2	Grid refinement of advected Gauss curve in 12 m tube. AUSM ⁺ -up.	51
5.3	Grid refinement of advected Gauss curve in 12 m tube. Lax-Friedrichs.	52
5.4	Grid refinement of advected Gauss curve in 12 m tube. MUSCL-FORCE.	53
5.5	Shock tube problem solved with MUSCL-AUSM ⁺ -up, effect of grid refinement.	55
5.6	Shock tube, comparison of MUSCL-AUSM ⁺ -up and MUSCL-FORCE, 4,000 cells.	56
5.7	Shock tube, comparison of speed of sound, MUSCL-AUSM ⁺ -up and MUSCL-FORCE, 4,000 cells.	58
5.8	Depressurization of pipe solved with AUSM ⁺ -up, 1,000 cells. $t = 0.2$ s.	62
5.9	Comparison of depressurization case, solved with MUSCL-AUSM ⁺ -up and MUSCL-FORCE, 1,000 cells. $t = 0.2$ s.	64
5.10	Depressurization of pipe, MUSCL-AUSM ⁺ -up compared to MUSCL-FORCE, 1,000 cells. $t = 7.4$ s.	65
5.11	Depressurization of pipe solved with MUSCL-AUSM ⁺ -up, 1,000 cells. $t = 0.2$ s. Effect of grid refinement.	66

List of Tables

5.1	1-norm error and convergence rate for advected gas volume fraction in 12 m tube. AUSM ⁺	49
5.2	1-norm error and convergence rate for advected gas volume fraction in 12 m tube. MUSCL-AUSM ⁺ (conserved variables, minmod-limiter).	49
5.3	1-norm error and convergence rate for advected gas volume fraction in 12 m tube. MUSCL-AUSM ⁺ (s, p, u , minmod-limiter).	50
5.4	1-norm error and convergence rate for advected gas volume fraction in 12 m tube. MUSCL-AUSM ⁺ (s, p, u , Van Leer-limiter).	50
5.5	1-norm error and convergence rate for advected gas volume fraction in 12 m tube. AUSM ⁺ -up.	51
5.6	1-norm error and convergence rate for advected gas volume fraction in 12 m tube. MUSCL-AUSM ⁺ -up.	51
5.7	1-norm error and convergence rate for advected gas volume fraction in 12 m tube. Lax-Friedrichs.	52
5.8	1-norm error and convergence rate for advected gas volume fraction in 12 m tube. MUSCL-FORCE.	53
5.9	Initial conditions for shock tube test.	54
5.10	Run-times for depressurization test case. Run until $t = 0.2$ s.	67

Nomenclature

Abbreviations

2DS	2°C scenario
AUSM	Advection upstream splitting method
BC	Boundary condition
CCS	Carbon capture and storage
CFD	Computational fluid dynamics
CFL	Courant-Friedrichs-Lewy
EOS	Equation of state
FDM	Finite difference method
FORCE	First ordered centered
FVM	Finite volume method
HEM	Homogeneous equilibrium model
IEA	International Energy Agency
LF	Lax-Friedrichs
MUSCL	Monotonic upstream-centered schemes for conservation laws
ODE	Ordinary differential equation
PDE	Partial differential equation
RK	Runge-Kutta
SLAU	Simple low-dissipation AUSM
SSP	Strong stability preserving
TVD	Total variation diminishing

Greek letters

α	Volume fraction
β	AUSM ⁺ parameter
δ	Slope
ϵ	Gauss curve parameter
ζ	AUSM ⁺ parameter

λ	Eigenvalue	
ρ	Mixture density	kg/m^3
σ	AUSM ⁺ -up parameter	
ψ	Vector of convected terms	
ω	Slope limiting function	

Latin letters

A	Jacobian matrix	
<i>a</i>	Gauss curve parameter	
<i>b</i>	Gauss curve parameter	
\mathcal{C}	Gauss curve parameter	
<i>c</i>	Speed of sound	m/s
\mathcal{E}	Error	
<i>E</i>	Total specific energy	J/kg
<i>e</i>	Specific internal energy	J/kg
F	Flux vector	
f	Numerical flux function	
f_c	Speed of sound scaling function	
<i>H</i>	Total specific enthalpy	J/kg
<i>K</i>	Coefficient	
<i>L</i>	Discrete spacial operator	
\mathcal{M}	Split Mach number	
<i>M</i>	Mach number	
\mathcal{P}	Split pressure	
<i>P</i>	Norm order	
<i>p</i>	Pressure	Pa
<i>q</i>	Value of variable in a coarse grid	
<i>Q</i>	Calue of variable in reference grid	
<i>R</i>	Convergence rate	
<i>r</i>	Ratio of grid sizes	
<i>s</i>	Order of accuracy	
<i>t</i>	Time	s
U	Vector of conserved variables	
<i>u</i>	General variable	
<i>v</i>	Velocity	m/s
<i>x</i>	Length coordinate	m

Superscripts

c	Convective terms
L	Left side of cell face
LF	Lax-Friedrichs flux
n	Time step index
p	Pressure terms
R	Right side of cell face
RI	Richtmyer flux
-	Mean

Subscripts

co	Relating to Mach number cut-off value
g	Gaseous phase
i	Spatial index
IM	Last cell in spatial domain
L	Left
l	Liquid phase
N	General component of multiphase flow
o	Reference value
p	Pressure diffusion term
R	Right
s	Solid phase
u	Velocity diffusion term
∞	Free-stream value

Chapter 1

Introduction

This chapter outlines the background for carbon capture and storage, CO₂ transport and the numerical simulation of CO₂ in pipes. Further it presents the structure of the thesis, provides background on the hardware and software utilized to run simulations, and gives acknowledgements of contributing partners.

1.1 Background

Carbon capture and storage (CCS) has over the past decades emerged as a possible key contributor to reducing carbon dioxide emissions. In the 2 °C scenario (2DS) presented by the International Energy Agency (IEA), CCS is estimated to contribute to 17% of reduced CO₂ emissions required by 2050 [9]. In the 2DS, almost 6 billion tonnes of CO₂ will have to be captured in that year [10].

The biggest target area for CCS is fossil-fueled power generation, but other industrial processes such as cement manufacture, iron and steel making produce large amounts of CO₂ and can be fitted with capture technologies [3]. The latter mentioned emitters account for 45% of captured CO₂ by 2050 in the 2DS [9].

Fossil-fueled power stations are believed to be a necessary part of the future energy mix for two reasons. Firstly due to the unlikeliness of a complete transition to renewables. In 2050, 43% of primary energy comes from fossil fuels [10] in the 2DS. The second reason, is the ability of gas and coal power plants to adjust power production quickly should a change in demand, or irregular supply of e.g. wind power, require it [3].

For the latter reason mentioned above, CCS also serves as a viable option to storing energy produced from renewable sources. Storage of energy generated from renewables is possible a way of securing constant clean energy from sources such as wind and solar power, even in periods of little wind or little sun. However, since gas and coal power plants can on short notice adjust power production, such power plants with CCS technology installed could provide an increased amount of cleaner energy than conventional gas and coal power plants, in periods of low production of renewable energy.

CCS consists of three different stages. These are the capture stage, the transport stage

and the storage stage. CO₂ requires suitable geological formations to keep it stored underground for a sufficiently long time, and so this means that extensive transport solutions will be a key part of any large-scale CCS operation. Out of all possible CO₂ transport options, such as pipeline, road, ship and rail, transporting CO₂ via pipeline is considered to be the most cost effective one under normal CCS operation, unless the CO₂ needs to be transported over large bodies of water or over distances of more than 1000 km [3].

1.1.1 CO₂ transport

Today, significant networks of pipelines supplying CO₂ for enhanced oil recovery (EOR) purposes are already in place. In the United States and Canada, more than 3000 km of currently operational CO₂ pipelines exist [8]. A large portion of these pipelines are found in the southern U.S., and they are primarily found onshore. The technology required for CO₂ pipeline transport is in other words mature enough for full-scale employment, but research is being performed in order to gain a better understanding of potential safety risks and possible efficiency improvements that could be implemented in the pipeline systems. One concern related to the normal operation of CO₂ pipelines is how trace chemical elements affect both flow properties and the corrosion of pipes [27].

Further, current research addresses how pipelines will handle cracks, leakages and depressurization. Should a crack occur it may propagate and cause a running fracture. Investigations show that cracks may propagate in the case of CO₂ transport, where they would not propagate if the transported medium were methane [1].

Another concern is the effect of cooling due to depressurization. CO₂ transported in pipelines is compressed to supercritical fluid or to a liquid state. Operating pressures of existing CO₂ pipelines are in the range 8.5 to 21MPa. At these pressures the CO₂ is in a dense phase for normal operating temperatures [3]. In the case of a depressurization, phase change will occur and the minimum temperature obtained during such an incident is of great interest, as temperatures might be reached at which some steels become brittle [7].

1.2 Thesis aim and relevance

This thesis work has been conducted with support from BIGCCS through the guidance and supervision given by BIGCCS project members. BIGCCS is an international research center managed by SINTEF Energy Research. Part of the threefold scientific objective of the organization is the focus on CO₂ transport, and the research group aims to *improve the fundamental understanding of the interaction between the mechanical and fluid dynamical behavior* of CO₂ pipelines in order to develop a coupled fluid-material fracture assessment model [20].

Thus this thesis aims to evaluate how appropriate the use of the advection upstream splitting method (AUSM) family of schemes is to simulate two-phase flow of CO₂ in pipes, and specifically how well suited the scheme is in combination with the homoge-

neous equilibrium model (HEM) and Span-Wagner equation of state. These models and numerical schemes are described in detail in subsequent chapters.

1.3 Thesis outline

This thesis first introduces the background for CCS, CO₂ transport and the purpose of computational modeling of CO₂ flow in pipes. In Chapter 2, multiphase flow and specifically the homogeneous equilibrium model (HEM) are presented.

Chapter 3 gives a thorough walkthrough of several of the key components of numerical methods for fluid dynamics. It describes the finite volume method, MUSCL-reconstruction, time integration methods, as well as accuracy and stability of the finite volume method. It further describes the AUSM family of numerical flux functions, as well as the FORCE and Lax-Friedrichs schemes.

Chapter 4 gives an introduction to thermodynamics and the Span-Wagner equation of state, whereas Chapter 5 presents the main results obtained by running test cases with the developed numerical tool. Main conclusions and suggested further work can be found in Chapter 6.

1.4 Numerical simulation framework

All simulations presented in this thesis were performed with programs written in Fortran by the author. The Span-Wagner equation of state library was provided by SINTEF Energy Research. All programs were compiled using the GNU Fortran compiler, GFortran. Where computational times are specified, the simulations were run in a Linux guest environment on a 3.7 GHz Quad-Core Intel Xeon E5 Mac Pro.

1.5 Acknowledgments

This thesis has been produced with support from the BIGCCS Centre, performed under the Norwegian research program Centres for Environment-Friendly Energy Research (FME). The support provided by BIGCCS includes guidance and supervision funded by the organization. BIGCCS is managed by SINTEF Energy Research, which has provided guidance as well as the thermodynamic library used in this thesis work. The author further acknowledges the following partners for their contributions to the BIGCCS research centre: Gassco, Shell, Statoil, TOTAL, GDF SUEZ and the Research Council of Norway (193816/S60).

The thesis is the author's final work at the Norwegian University of Science and Technology, and was produced at the Department of Energy and Process Engineering (EPT). EPT provided supervision, guidance and the equipment and facilities necessary to perform simulations and produce the thesis.

Chapter 2

Multiphase flow

This chapter first introduces some key concepts related to multiphase flow. The need for multiphase flow models is briefly discussed. Then the model utilized in the work presented in this thesis – the homogeneous equilibrium model (HEM) – is described in greater detail.

2.1 Key concepts

The term multiphase flow can be taken to mean different things depending on the setting in which the term is used. In this thesis the term is used to describe fluid flow with at least two different phases or components. Further, the phases or components are separated at a scale above the molecular level, as in accordance with the description in [4, Sec. 1.1].

The separate components of a multiphase flow have separate volume fractions, denoted by the letter α . Thus, considering N components of the flow, the sum of all volume fractions is

$$\sum_{j=1}^N \alpha_j = 1. \quad (2.1)$$

2.2 Multiphase flow models

Flow models serve the purpose of representing the characteristic properties of a fluid flow and predicting how this flow will behave. The exploration of such models through experiments, mathematical and computational analysis helps predict the nature of actual, real-life flow situations. Experiments will in a number of cases be impractical and expensive, and so mathematical analysis and the ability to numerically simulate flow behavior are greatly valued in a range of fields involving fluid dynamics. Thus the formulation of an appropriate flow model to be investigated using these methods is of key importance.

The two-fluid model can be used to model both disperse and separated flows [4, Sec. 1.1]. In the former case, the phase with the disperse particles is treated as a continuous phase. The two-fluid model makes use of two sets of conservation equations for the two fluids, and interaction terms model the exchange of mass, momentum and energy between the two fluids. The two-fluid model can also be extended to model more than two components.

A full, three dimensional simulation of a multicomponent flow situation using the two-fluid model is computationally expensive. A large portion of the added computational power required to perform such a simulation is due to the complexity of, and fine grid required for, calculating the exchange of mass, momentum and energy at the component interfaces. Hence, it is common to make certain assumptions about the flow in order to simplify and speed up simulations.

Two key assumptions made in this thesis is neglecting viscous terms and treating all problems as one-dimensional. The latter assumption is often used when simulating flow in pipes. See Chapter 5 for a more detailed description of the physical interpretation of test cases. Further simplifications can also be made, to the point where the flow models obtained are no longer known as two-fluid models. The flow model used for the simulations presented in this report is known as the homogeneous equilibrium model. It is introduced in the succeeding section.

2.3 Homogeneous equilibrium model

The homogeneous equilibrium model (HEM) is one of the simplest multiphase flow models. It governs inviscid multiphase flow. Homogeneous flows assume no relative motion between the phases. Further, the assumption of equilibrium means that phase change, transfer of volume and heat transfer between the phases happen instantaneously. Hence there is thermodynamic equilibrium. This in turn entails equal chemical potential, pressure and temperature for the phases.

The resulting equations are of a form similar to the Euler equations for single phase flow. The set of partial differential equations (PDEs), in conservation form, read

$$\frac{\partial \rho}{\partial t} + \frac{\partial(\rho v)}{\partial x} = 0, \quad (2.2)$$

$$\frac{\partial(\rho v)}{\partial t} + \frac{\partial(\rho v^2 + p)}{\partial x} = 0, \quad (2.3)$$

$$\frac{\partial(\rho E)}{\partial t} + \frac{\partial(v(\rho E + p))}{\partial x} = 0. \quad (2.4)$$

These three equations govern the conservation of mass, momentum and energy, respectively.

The density, ρ , is the mixture density, given by

$$\rho = \sum_{j=1}^N \alpha_j \rho_j. \quad (2.5)$$

for N components of a fluid.

The term E is the total specific energy, consisting of internal energy and kinetic energy per unit mass

$$E = e + \frac{v^2}{2}. \quad (2.6)$$

Equations (2.2)–(2.4) can be grouped using the following two vectors

$$\mathbf{U} = \begin{bmatrix} \rho \\ \rho v \\ \rho E \end{bmatrix}, \quad (2.7)$$

$$\mathbf{F} = \begin{bmatrix} \rho v \\ \rho v^2 + p \\ (\rho E + p)v \end{bmatrix}. \quad (2.8)$$

The system of equations can hence be written in the form

$$\frac{\partial}{\partial t} \mathbf{U} + \frac{\partial}{\partial x} \mathbf{F}(\mathbf{U}) = 0. \quad (2.9)$$

The vector \mathbf{U} is referred to as the vector of conserved variables, whereas the vector \mathbf{F} is referred to as the flux vector.

The system in Equation (2.9) can be written in quasi-linear form

$$\frac{\partial \mathbf{U}}{\partial t} + \mathbf{A}(\mathbf{U}) \frac{\partial \mathbf{U}}{\partial x} = 0. \quad (2.10)$$

Here, $\mathbf{A}(\mathbf{U}) = \frac{\partial \mathbf{F}}{\partial \mathbf{U}}$ is the Jacobian matrix of the system. The three eigenvalues of this matrix are $\lambda_1 = v - c$, $\lambda_2 = v$ and $\lambda_3 = v + c$ [32, Sec. 3.1.1].

2.3.1 Speed of sound

A special emphasis must be given to evaluating the speed of sound for multiphase flows modeled with HEM. The discussion of the accuracy of the evaluated speed of sound for two phase models is interesting in itself and the effect of relaxing different parameters in two-fluid models can be seen for instance in [5].

However, because the AUSM family of numerical flux functions evaluate the flux using a formulation that includes the speed of sound, the way the thermodynamic function evaluates the speed of sound for the homogeneous equilibrium model is of special interest. Thus, a simple evaluation of the speed of sound for a liquid-vapor mixture on the saturation line, with varying composition, is presented here as a backdrop for the discussion in Chapter 5.

The speed of sound is calculated from the well-known equation

$$c = \sqrt{\left. \frac{\partial p}{\partial \rho} \right|_s}, \quad (2.11)$$

where the subscript s indicates that the derivative is taken at constant entropy. For details on the calculation of speed of sound in the two-phase region, see [7].

Figure 2.1 shows the speed of sound evaluated on the saturation line using the Span-Wagner equation of state (see Section 4.2) for an arbitrarily chosen temperature 280.0 K. The corresponding pressure at this temperature is 4.16 MPa. Notice the sharp discontinuity that occurs as some gas is introduced into the liquid. This is a well established phenomenon for a fully relaxed model, and it is due to the simultaneous equilibrium assumptions described in the introduction to Section 2.3. Similarly to the discontinuity observed as one moves from liquid to liquid-vapor, a discontinuity can also be observed as one transitions from liquid-vapor to vapor.

Equilibrium constraints always reduce the speed of sound, but the sharp discontinuities only occur for fully relaxed models [5]. Such discontinuities are not believed to be physically correct [2].

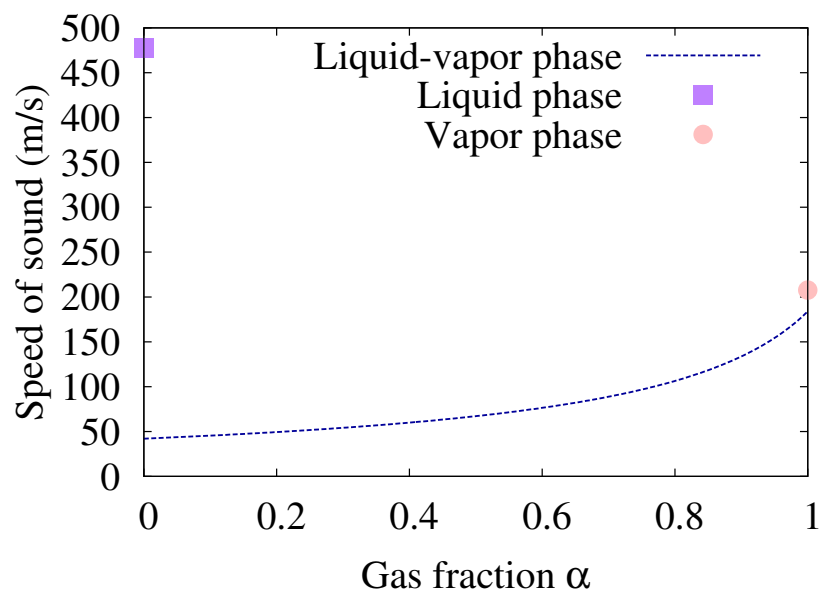


Figure 2.1: Speed of sound at evaluated saturation pressure (4.16 MPa) for temperature 280.0 K.

Chapter 3

Numerical methods for fluid dynamics

This chapter presents the numerical procedure used to solve the flow model presented in this thesis. The general discretization method utilized, the finite volume method, is presented, along with the methods utilized for finding the numerical flux, as well as time integration methods.

Further the MUSCL method of reconstruction of variables is presented. This method allows for higher spatial accuracy. General ideas behind simulation accuracy, stability, error and convergence are presented.

3.1 Finite volume method

In computational fluid dynamics (CFD), a commonly utilized discretization method is the finite volume method (FVM). This method makes use of a set of control volumes, also called cells, that together form the domain, the total region for which physical properties are to be calculated. A domain can be considered as one-, two- or three-dimensional. All the simulations performed in this thesis were carried out for a domain discretized in one dimension. Since these simulations consider pipe flow, the finite volumes will be sections of the pipe in the shape of cylinders, the size of which depend on the length of the pipe and the number of finite volumes.

The finite volume method allows for the formulation of schemes that are based on the conserved variables. This is desirable and often a necessity when solving problems where shocks may occur. There exist certain special procedures, such as shock-fitting and adaptive primitive-conservative schemes, that can serve as alternatives to conservative methods, but only a conservative method is guaranteed to converge to a weak solution of the conservation law [15, Sec. 12.10].

The system of one-dimensional conservation laws considered can be written in the following form. This corresponds to the form seen in Equation (2.9) in Section 2.3.

$$\frac{\partial \mathbf{U}}{\partial t} + \frac{\partial \mathbf{F}(\mathbf{U})}{\partial x} = 0. \quad (3.1)$$

The system of equations can be written in integral form, considering the control volume i from x_L to x_R ,

$$\frac{d}{dt} \int_{x_L}^{x_R} \mathbf{U}(x, t) dx = \mathbf{F}(\mathbf{U}(x_L, t)) - \mathbf{F}(\mathbf{U}(x_R, t)). \quad (3.2)$$

Cell averages of the following form are introduced.

$$\mathbf{U}_i(t) \approx \frac{1}{\Delta x} \int_{x_L}^{x_R} \mathbf{U}(x, t) dx. \quad (3.3)$$

Within the control volume, the conserved quantities are thus no longer functions of x . The system with cell averaged conserved quantities is then given by

$$\frac{d}{dt} \Delta x \mathbf{U}_i(t) = \mathbf{F}(\mathbf{U}(x_L, t)) - \mathbf{F}(\mathbf{U}(x_R, t)). \quad (3.4)$$

Denoting $\mathbf{F}(\mathbf{U}(x_L, t)) = \mathbf{F}(\mathbf{U}_{i-1/2})$ and $\mathbf{F}(\mathbf{U}(x_R, t)) = \mathbf{F}(\mathbf{U}_{i+1/2})$, one gets the ODE

$$\frac{d}{dt} \mathbf{U}_i = \frac{\mathbf{F}(\mathbf{U}_{i-1/2}) - \mathbf{F}(\mathbf{U}_{i+1/2})}{\Delta x}. \quad (3.5)$$

Since the values of the conserved variables are only known in the cells and not at the cell faces, where the fluxes are evaluated, an approximation of these fluxes is needed. This is done by use of a numerical flux function. The AUSM family of numerical schemes presented in Section 3.5 serves this purpose, and so does the first ordered centered (FORCE) scheme presented in Section 3.7. The numerical flux function is denoted by a lowercase \mathbf{f} instead of the uppercase \mathbf{F} . One can then write

$$\frac{d}{dt} \mathbf{U}_i = \frac{(\mathbf{f}_{i-1/2} - \mathbf{f}_{i+1/2})}{\Delta x}. \quad (3.6)$$

Figure 3.1 shows an illustration of the discretized domain, with the location of the numerical flux function indicated on the interface between the cells.

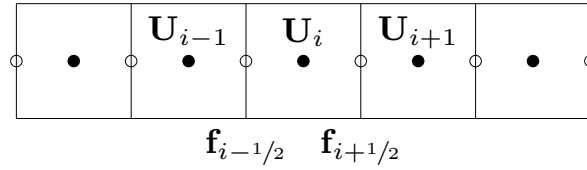


Figure 3.1: One-dimensional discretization used in calculations. Control volumes around each node, where cell-averages are stored, and locations of the faces, where the numerical fluxes are calculated, indicated.

Equation (3.6) for all cells i constitutes a system of ordinary differential equations (ODEs). This form of the system is known as semi-discrete due to the discretized spatial derivative being present in the equations along with the non-discretized time derivative [14, Sec. 17]. This formulation allows solving the time derivative with regular ODE solvers. Writing a system of PDEs on this form in order to solve with an ODE solver is often referred to as the method of lines.

Formulating a system as semi-discrete equations is also helpful when trying to separate the concepts of spatial and temporal accuracy. These concepts are explored further in Sections 3.2 and 3.4.

3.2 Accuracy and stability

The purpose of this section is to highlight certain issues related to accuracy that are important to present in order to explain the motivation behind some of the numerical schemes utilized. The current section does not present a comprehensive overview of the various sources of error commonly found in CFD. For detailed information on this topic, see for example [15, Ch. 8].

3.2.1 Determining error, order of accuracy and rate of convergence

A numerical scheme with a given order of accuracy, s , is expected to have an error, compared to the exact solution, that is of order Δx^s [15, Ch. 8.5]. Thus if a scheme is said to be second order, i.e. $s = 2$, the error of a numerical solution should be reduced by a factor four if the computational cell size is reduced from Δx to $\Delta x/2$.

The order of accuracy can be determined for a given scheme by using Taylor expansions for the fluxes in a single cell and determining the truncation error, in a fashion similar to the way these are evaluated for finite difference methods (FDM) [13]. The obtained order of accuracy should correspond to the errors calculated and corresponding rates of convergence.

A value for the error of a numerical solution can be found using a norm. A generalized formula for a standard set of norms, known as the p -norms is given in [15, Sec. 8.1.1].

Here, the p -norms shall be denoted using an uppercase P to avoid any confusion with pressure, p . Thus, the P -norms can be written as

$$\|\mathcal{E}\|_P = \left(\Delta x \sum_{i=-\infty}^{\infty} |\mathcal{E}_i|^P \right)^{(1/P)}. \quad (3.7)$$

Typical choices of norms include $P = 1$, $P = 2$ and letting $P \rightarrow \infty$. These norms are known as the 1-norm, 2-norm and infinity norm, respectively. In the present work, all error calculations have been performed using the 1-norm. This is common for conservation problems. Equation (3.7) is in discrete form and sums the modulus of the local error in each cell to get one value representing the error of the solution as a whole. The local error is given by

$$\mathcal{E}_i = q_i - Q_i. \quad (3.8)$$

Here q denotes the numerically calculated value, which is being compared to a reference value Q . The reference value is ideally obtained analytically if possible, but typically it is found using established methods and/or very fine grids. In case the values are obtained for different grid sizes, the reference values must be adapted so that the reference grid and the coarse grid are of equal size. This can for example be done by using simple arithmetic averaging of reference values.

The convergence rate can be calculated according to the following formula

$$R = \frac{\log\left(\frac{\text{err}(\Delta x)}{\text{err}\left(\frac{\Delta x}{r}\right)}\right)}{\log(r)}. \quad (3.9)$$

The convergence rate, R , is a measure of error decrease. It shows the effect grid refinement has on approaching the reference solution. Notice that *err* denotes the error calculated using a norm of choice for a given value of the cell spacing Δx . This value is then compared to the error calculated for a grid that has been refined by a factor r . The convergence rate should, upon continued grid refinement, approach the known order of the schemes utilized.

3.2.2 Increasing the order of accuracy

AUSM schemes and several other schemes, such as the Godunov scheme and approximate Riemann solvers, construct the numerical flux function from the values of \mathbf{U} in the cells immediately adjacent to the cell face in question. Thus

$$\mathbf{f}_{i+1/2} = \mathbf{f}_{i+1/2}(\mathbf{U}_i, \mathbf{U}_{i+1}). \quad (3.10)$$

Such schemes are known to be first order accurate, since they approximate the solutions in the cells by constants.

Using e.g. second order schemes, such as Lax-Wendroff or Beam-Warming methods that are not total variation diminishing (TVD), is not preferable when solving problems with discontinuities [15, Sec. 8.5]. For this reason, a better method used to obtain increased accuracy is to reconstruct the variable values that serve as input to the flux function of a TVD method. Such a procedure is outlined in Section 3.3.

3.2.3 Courant-Friedrichs-Lewy number

The Courant-Friedrichs-Lewy number (CFL), also called the Courant number, is defined as

$$\text{CFL} = \frac{\lambda_{\max}}{\Delta t / \Delta x}. \quad (3.11)$$

λ_{\max} is the largest eigenvalue modulus of the Jacobian matrix of the system of equations considered. The CFL number is a dimensionless number that serves as a stability condition when performing calculations. Typically, the stability condition is $\text{CFL} \leq 1$. This ensures that the maximum wave speed, λ_{\max} , does not propagate any information a distance greater than a cell length, Δx , during one time step.

In practice, calculations are often performed with a specified CFL number. This way the time step size is set dynamically in each time step, ensuring that the CFL-condition is fulfilled.

All calculations in this thesis were performed with a CFL value of 0.5. For this particular CFL value, certain time integration methods in combination with several numerical flux functions and MUSCL reconstruction, with different slope limiters, have the total variation diminishing (TVD) property [11]. Thus for $\text{CFL}=0.5$ the CFL number can remain unchanged for different flux functions and limiters, which is beneficial when comparing these.

Various methods for performing time-integration, or stepping in time, are presented in Section 3.4. This Section also explains the TVD property. MUSCL reconstruction and slope limiters are explained in Section 3.3.

3.3 MUSCL

As can be seen from Equation (3.3), the basic approach in the finite volume method is to create a cell average of variables. This way, a variable has a single value in a single cell or control volume, as illustrated in Figure 3.2.

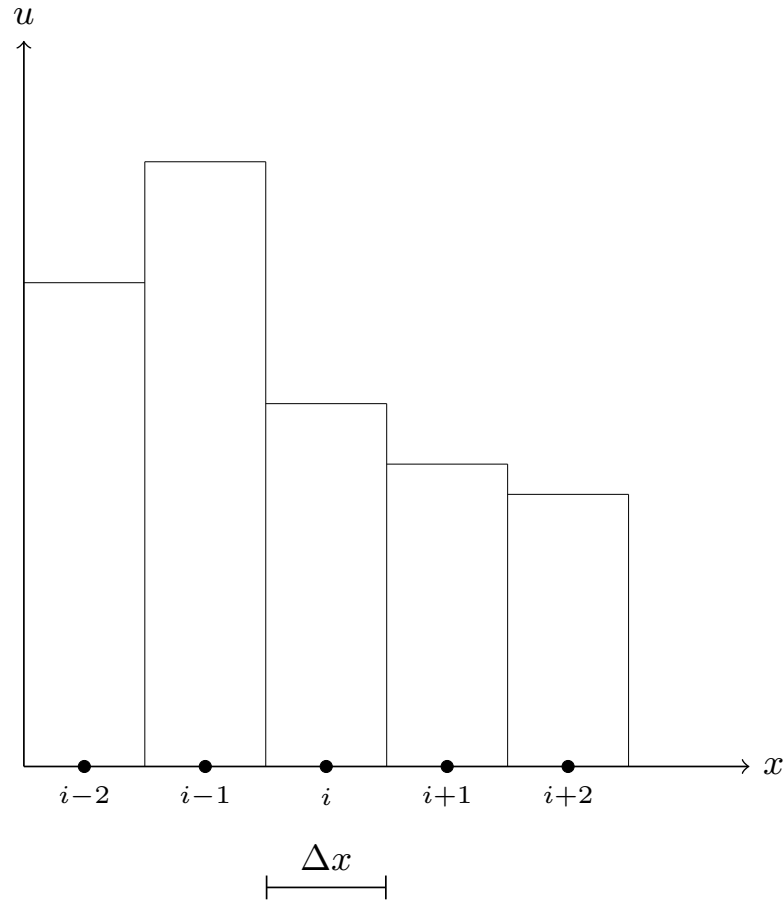


Figure 3.2: Illustration of cell average of arbitrary variable in grid.

As mentioned in Section 3.2.2, using schemes that increase the order of accuracy directly is disadvantageous for problems with discontinuities. For this reason, it is common to perform a reconstruction of the variables in a computational cell. The method used to do this is known as monotonic upstream-centered schemes for conservations laws (MUSCL) [34].

The reconstruction of variables creates a variation in the variable values within the cells, based on the values of neighboring cells. The reconstruction is piecewise, as can be seen in Figure 3.3. The reconstruction performed for all MUSCL schemes used in this thesis work has made use of linear reconstruction, similar to what is shown in Figure 3.3. It is however possible to use higher order reconstruction, such as parabolic reconstruction, for increased accuracy.

Commonly, a set of state variables are reconstructed, from which all other variables necessary for computing the flux are calculated. The calculations presented in this thesis have either reconstructed the conserved variables, or pressure, temperature and entropy. It is also possible to perform a direct, piecewise reconstruction of the flux

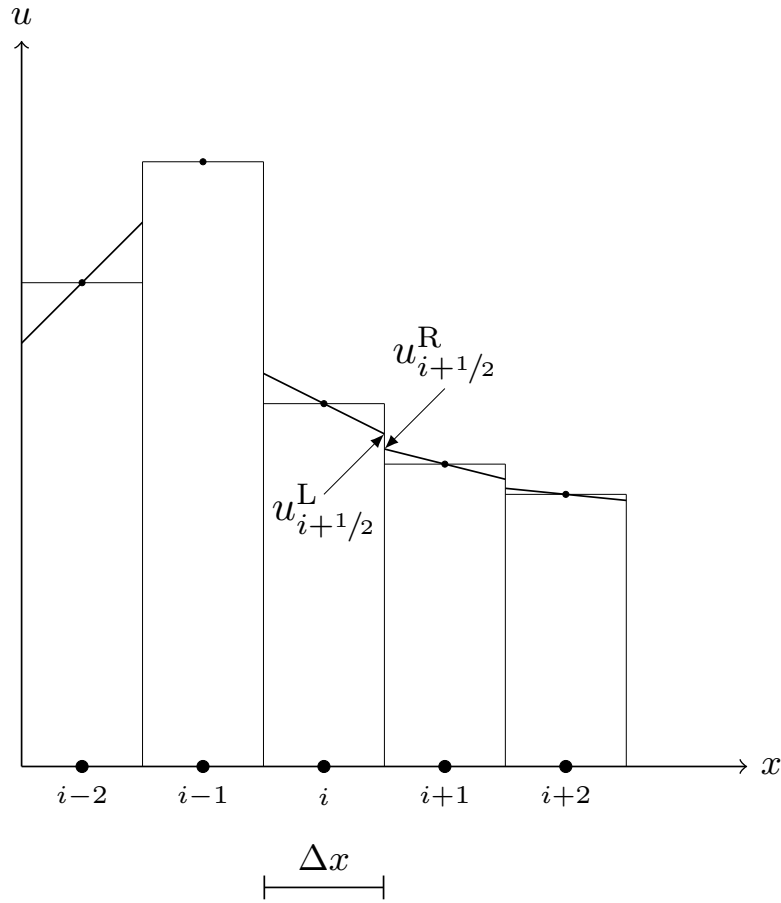


Figure 3.3: Illustration of linearly reconstructed cell variables.

[25, Sec. 4.4.11], but this approach sees infrequent use and has not been used in the present work.

The numerical flux based on MUSCL reconstructed variables is given by

$$\mathbf{f}_{i+1/2} = \mathbf{f}_{i+1/2}(\mathbf{U}_{i+1/2}^L, \mathbf{U}_{i+1/2}^R). \quad (3.12)$$

Here,

$$u_{i+1/2}^L = u_i + \delta u_i \frac{\Delta x_i}{2}, \quad (3.13)$$

$$u_{i+1/2}^R = u_{i+1} - \delta u_{i+1} \frac{\Delta x_{i+1}}{2}. \quad (3.14)$$

Note that the notation δu_i denotes a limited slope based on the slopes calculated from the neighboring cell values of u . Thus, one has,

$$\delta u_{i+1/2} = \frac{u_{i+1} - u_i}{x_{i+1} - x_i} \quad (3.15)$$

and

$$\delta u_{i-1/2} = \frac{u_i - u_{i-1}}{x_i - x_{i-1}}. \quad (3.16)$$

The use of so-called slope limiters is a crucial part of the MUSCL approach. Without the use of such slope limiters oscillations could occur and the total variation (TVD) property would not be fulfilled [21]. See Section 3.4 for a description of the TVD condition. Different slope limiters exist, and a slope limiting function will here be denoted by the letter ω . Thus the limited slope is defined to be

$$\delta u_i = \omega(\delta u_{i-1/2}, \delta u_{i+1/2}) \quad (3.17)$$

Two different slope limiters have been utilized in the present work, the minmod limiter and the Van Leer limiter. They are given by

$$\omega_{\text{minmod}} = \begin{cases} a & \text{if } |a| \leq |b| \text{ and } ab > 0, \\ b & \text{if } |b| \leq |a| \text{ and } ab > 0, \\ 0 & \text{if } ab \leq 0. \end{cases} \quad (3.18)$$

$$\omega_{\text{van Leer}} = \begin{cases} \frac{ab+|ab|}{a+b} & \text{if } a + b \neq 0, \\ 0 & \text{if } a + b = 0. \end{cases} \quad (3.19)$$

Notice how the slope in the case of extrema, for both limiters, is set to zero and the original first order scheme will be recovered. The same is true when at least one slope is zero for minmod, and when both slopes are zero for Van Leer.

3.4 Time integration methods

As pointed out in Section 3.1, solving equations in the form seen in Equation (3.6) can be done using the so-called method of lines. This allows for solving a system of PDEs

using a regular ODE solver. When choosing a time integration method, it can be preferable to choose a so-called strong stability preserving (SSP) Runge-Kutta (RK) method. Such methods preserve the total variation diminishing (TVD) property, positivity and the strong stability properties of the explicit Euler method presented in Section 3.4.1 [11].

The TVD condition requires for a scalar conservation law that the following inequality be true

$$\|u^{n+1}\| \leq \|u^n\| \quad (3.20)$$

when the norms are calculated using total variation (TV) norm, which is given by

$$\|u^n\|_{\text{TV}} = \sum_i |u_i^n - u_{i-1}^n|. \quad (3.21)$$

When a numerical scheme produces a solution of a scalar conservation problem that is TVD, the extension of such a scheme to a system of conservation laws does not necessarily guarantee that the solution of the system is TVD. Still, the numerical scheme that possesses the TVD property can in most cases be extended to be used on a system of equations, it will be called TVD and will still in most cases avoid spurious oscillations near discontinuities [11].

When performing time integration of an equation in the form of Equation (3.6), it is common to write the equation on the following form:

$$\frac{d}{dt} \mathbf{U} = L(\mathbf{U}). \quad (3.22)$$

\mathbf{U} contains all the vectors of cell-averaged conserved variables, for all cells in the spatial domain. Thus $\mathbf{U} = [\mathbf{U}_1, \dots, \mathbf{U}_{\text{IM}}]^\top$. $L(\mathbf{U})$ is known as the discrete spatial operator and it contains the corresponding fluxes for each cell, i.e. a vector of $(\mathbf{f}_{i-1/2} - \mathbf{f}_{i+1/2}) / \Delta x$ for all cells. When presenting the time integration methods used, they will be presented using the form seen in Equation 3.22, as it allows for a compact presentation of the time integration steps. Note that the equation is in semi-discrete form, which allows for solving using a regular ODE solver, such as thos presented in Sections 3.4.1 and 3.4.2.

3.4.1 Explicit Euler method

Whenever a first order accurate solution is presented in this thesis, the time integrator used will have been the explicit or forward Euler method. Based on the form seen in Equation (3.22), this method can be written as

$$\mathbf{U}^{n+1} = \mathbf{U}^n + \Delta t L(\mathbf{U}^n). \quad (3.23)$$

3.4.2 Heun's method

Heun's method, a second order accurate method, known as SSP22 in [11], has been used with all MUSCL-reconstructed simulations. This method is given by

$$\mathbf{U}^{(1)} = \mathbf{U}^n + \Delta t L(\mathbf{U}^n), \quad (3.24)$$

$$\mathbf{U}^{n+1} = \mathbf{U}^n + \frac{\Delta t}{2} \left(L(\mathbf{U}^n) + L(\mathbf{U}^{(1)}) \right). \quad (3.25)$$

Heun's method is the optimal second order accurate, two-stage method [29]. An optimal method is a method that gives the largest SSP coefficient for all methods achieving the same order of accuracy using the same number of steps. The SSP coefficient is a CFL-like condition, but the two are not the same. For details on the SSP coefficient, see [11].

3.4.3 Other time integration methods

Other methods, such as the optimal third order, three-stage method [29] and the Optimal SSP33(2R) method [11] have been implemented and tested, but since these methods are computationally more expensive and third order accuracy is not necessary for any of the simulations performed, these methods were not used for any of the presented results.

3.5 AUSM family

The Advection Upstream Splitting Method (AUSM) was first introduced in 1993 [18]. It is an upwind, flux splitting method. Details on the development and the motivation behind the original scheme may be found in [18].

The original scheme, as well as its two successors, AUSM⁺ and AUSM⁺-up, have the advantage of not requiring calculations of the eigenvalues or eigenvectors of the system of equations in question. Thus, since they do not require an analytical evaluation of the eigensystem of the Jacobian matrix, this allows for a comparably easy extension to multiphase flow models [19].

The original AUSM scheme will not be presented in detail in this thesis, but its sequel AUSM⁺ will. The AUSM⁺ is a relatively simple extension to AUSM, which can actually be viewed as a special case of AUSM⁺ [16]. This will be explained briefly in Section 3.5.1.

The key idea behind the AUSM schemes is the separate discretization of the convective flux terms and the pressure flux terms. This distinction is due to the pressure propagation being governed by the acoustic wave speeds. Thus the flux terms are split as follows

$$\mathbf{F} = \mathbf{F}^{(c)} + \mathbf{F}^{(p)}. \quad (3.26)$$

If one then considers the homogeneous equilibrium model (HEM), the flux is then split in these two vectors,

$$\mathbf{F} = \begin{bmatrix} \rho v \\ \rho v^2 + p \\ \rho H v \end{bmatrix} = \mathbf{F}^{(c)} + \mathbf{F}^{(p)} = v \begin{bmatrix} \rho \\ \rho v \\ \rho H \end{bmatrix} + \begin{bmatrix} 0 \\ p \\ 0 \end{bmatrix}. \quad (3.27)$$

H , the total specific enthalpy, is

$$H = e + \frac{p}{\rho} + \frac{v^2}{2}. \quad (3.28)$$

The numerical flux function is given by

$$\mathbf{f}_{\frac{1}{2}} = \mathbf{f}_{\frac{1}{2}}^{(c)} + \mathbf{f}_{\frac{1}{2}}^{(p)}. \quad (3.29)$$

The convected part can be written as

$$\mathbf{f}_{\frac{1}{2}}^{(c)} = M_{\frac{1}{2}} c_{\frac{1}{2}} \boldsymbol{\psi}_{L/R}. \quad (3.30)$$

The vector $\boldsymbol{\psi}$ does then, for HEM, contain the following terms: $\boldsymbol{\psi} = [\rho, \rho v, \rho H]^\top$. Notice the subscript L/R. This is where the upwind component of AUSM schemes enters. The cell from which information is to be used is decided by

$$(\bullet)_{L/R} = \begin{cases} (\bullet)_L, & \text{if } M_{\frac{1}{2}} \geq 0; \\ (\bullet)_R, & \text{otherwise.} \end{cases} \quad (3.31)$$

The pressure flux, for HEM, is given as $\mathbf{f}_{\frac{1}{2}}^{(p)} = [0, p_{\frac{1}{2}}, 0]^\top$.

The above formulas are true for AUSM, AUSM⁺ and AUSM⁺-up. Hence, it is the formulation of the face Mach number, $M_{\frac{1}{2}}$, the face speed of sound, $c_{\frac{1}{2}}$ and the face pressure term, $p_{\frac{1}{2}}$ that separate the schemes.

$M_{L/R}$ is based on the speed of sound at the cell face.

$$M_{L/R} = \frac{u_{L/R}}{c_{\frac{1}{2}}}, \quad (3.32)$$

The face speed of sound can simply be taken to be one of the following, as described in [16],

$$c_{\frac{1}{2}} = \frac{c_L + c_R}{2}, \quad (3.33)$$

$$c_{\frac{1}{2}} = \sqrt{c_L c_R}. \quad (3.34)$$

$$(3.35)$$

In all presented results, for calculations performed with AUSM⁺-up, the former formula has been used. For the original AUSM scheme, the face speed of sound was simply taken to be

$$c_{\frac{1}{2}} = \begin{cases} c_L, & \text{if } M_{\frac{1}{2}} \geq 0; \\ c_R, & \text{otherwise.} \end{cases} \quad (3.36)$$

The method of determining the face speed of sound presented in Equation (3.36) has not been used in any of the results presented, but is included for completeness.

The remaining components specific to AUSM⁺ and AUSM⁺-up will be described in Sections 3.5.1 and 3.5.2 respectively.

3.5.1 AUSM⁺

For all AUSM schemes, $M_{\frac{1}{2}}$ and $p_{\frac{1}{2}}$, are formulated based on split Mach numbers and pressures. For AUSM⁺ these are given as

$$M_{\frac{1}{2}} = \mathcal{M}^+(M_L) + \mathcal{M}^-(M_R), \quad (3.37)$$

$$p_{\frac{1}{2}} = \mathcal{P}^+(M_L) p_L + \mathcal{P}^-(M_R) p_R. \quad (3.38)$$

The split Mach numbers $\mathcal{M}_{(m)}^\pm$ are

$$\mathcal{M}^\pm(M) = \begin{cases} \frac{1}{2}(M \pm |M|) & \text{if } |M| \geq 1; \\ \pm \frac{1}{4}(M \pm 1)^2 \pm \beta(M^2 - 1)^2 & \text{otherwise.} \end{cases} \quad (3.39)$$

The split pressures are

$$\mathcal{P}^\pm(M) = \begin{cases} \frac{1}{2} \frac{(M \pm |M|)}{M} & \text{if } |M| \geq 1; \\ \frac{1}{4}(M \pm 1)^2(2 \mp M) \pm \zeta M(M^2 - 1)^2 & \text{otherwise.} \end{cases} \quad (3.40)$$

The parameters ζ and β can be tuned depending on the problem. Unless otherwise stated, the default values of $\beta = \frac{1}{8}$ and $\zeta = \frac{3}{16}$ have been used for the results presented in Chapter 5. The two parameters have the following constraints:

$$-\frac{1}{16} \leq \beta \leq \frac{1}{2}, \quad (3.41)$$

$$-\frac{3}{4} \leq \zeta \leq \frac{3}{16}. \quad (3.42)$$

As pointed out in [16], by setting the two parameters β and ζ equal to zero and applying Equation (3.36) one regains the original AUSM scheme.

3.5.2 AUSM⁺-up

AUSM⁺-up was published in [17] and is the second general extension to the original AUSM scheme. It introduces a slightly more complicated procedure to define the face pressures and Mach numbers, and in doing so the scheme introduces a few new parameters.

The mean local Mach number is given by

$$\bar{M}^2 = \frac{M_L^2 + M_R^2}{2} = \frac{u_L^2 + u_R^2}{2c_{\frac{1}{2}}^2}. \quad (3.43)$$

The reference Mach number, M_o , in turn makes use of the newly defined mean local Mach number and is given as

$$M_o^2 = \min(1, \max(\bar{M}^2, M_{co}^2)). \quad (3.44)$$

Here, the cut-off Mach number, M_{co} , should be $O(M_\infty)$. M_∞ is the free stream Mach number. For the case of low Mach number flow, the cut-off Mach number is suggested set to

$$M_{co} = \max(0.3, \frac{1}{2}M_\infty) \quad (3.45)$$

in [17]. In the case of no obvious free-stream Mach-number, the cut-off Mach number was set to 1.0. [24] suggests setting the cut-off Mach number to 10^{-4} , but as is discussed in [26], a higher cut-off Mach number is required for unsteady simulations, and 1.0 was chosen in accordance with [26]. For a further discussion on the choice of cut-off Mach number, see Chapter 5.

The scaling function, f_c , is defined to be

$$f_c = f_c(M_o) = M_o(2 - M_o). \quad (3.46)$$

The face Mach-number and pressure can be defined from this, and are for AUSM⁺-up constructed from higher order polynomials, as suggested in the original article [17].

$$\begin{aligned} M_{\frac{1}{2}} &= \mathcal{M}_{(4)}^+(M_L) + \mathcal{M}_{(4)}^-(M_R) + M_p \\ &= \mathcal{M}_{(4)}^+(M_L) + \mathcal{M}_{(4)}^-(M_R) - \frac{K_p}{f_c} \max(1 - \sigma \bar{M}^2, 0) \frac{p_R - p_L}{\rho_{\frac{1}{2}} c_{\frac{1}{2}}^2}, \end{aligned} \quad (3.47)$$

$$\begin{aligned} p_{\frac{1}{2}} &= \mathcal{P}_{(5)}^+(M_L)p_L + \mathcal{P}_{(5)}^-(M_R)p_R + p_u \\ &= \mathcal{P}_{(5)}^+(M_L)p_L + \mathcal{P}_{(5)}^-(M_R)p_R - K_u \mathcal{P}_{(5)}^+(M_L) \mathcal{P}_{(5)}^-(M_R) (\rho_L + \rho_R) (f_c c_{\frac{1}{2}}) (u_R - u_L). \end{aligned} \quad (3.48)$$

where $0 \leq K_p \leq 1$, $0 \leq K_u \leq 1$ and $\sigma \leq 1$.

The values used for the coefficients in the original article by Liou are the following:

$$K_p = 0.25 \quad (3.49)$$

$$K_u = 0.75 \quad (3.50)$$

$$\sigma = 1.0 \quad (3.51)$$

These parameters have been used for all simulation results presented in this thesis.

The density at the cell face is

$$\rho_{\frac{1}{2}} = (\rho_L + \rho_R)/2. \quad (3.52)$$

The split Mach numbers $\mathcal{M}_{(m)}^{\pm}$ are

$$\mathcal{M}_{(1)}^{\pm}(M) = \frac{1}{2}(M \pm |M|), \quad (3.53)$$

$$\mathcal{M}_{(2)}^{\pm}(M) = \pm \frac{1}{4}(M \pm 1)^2, \quad (3.54)$$

$$\mathcal{M}_{(4)}^{\pm}(M) = \begin{cases} \mathcal{M}_{(1)}^{\pm} & \text{if } |M| \geq 1; \\ \mathcal{M}_{(2)}^{\pm}(1 \mp 16\beta\mathcal{M}_{(2)}^{\mp}) & \text{otherwise.} \end{cases} \quad (3.55)$$

The split pressures are

$$\mathcal{P}_{(5)}^{\pm}(M) = \begin{cases} \frac{1}{M}\mathcal{M}_{(1)}^{\pm} & \text{if } |M| \geq 1; \\ \mathcal{M}_{(2)}^{\pm} \left((\pm 2 - M) \mp 16\zeta M \mathcal{M}_{(2)}^{\mp} \right) & \text{otherwise.} \end{cases} \quad (3.56)$$

Notice that the definition of the polynomials is the same as in Section 3.5.1, but the equations are restated here with the notation used in [17], which highlight the order of the polynomials. The parameters β and ζ are as in AUSM⁺ suggested to be in the range

$$-\frac{1}{16} \leq \beta \leq \frac{1}{2}, \quad (3.57)$$

$$-\frac{3}{4} \leq \zeta \leq \frac{3}{16}. \quad (3.58)$$

Once again the suggested values have been used.

$$\beta = \frac{1}{8} \quad (3.59)$$

$$\zeta = \frac{3}{16}(-4 + 5f_c^2). \quad (3.60)$$

Notice how ζ now depends on the value of f_c . Notice further in Equations (3.47) and (3.48) the pressure diffusion term M_p and the velocity diffusion term, p_u . At first glance, these two terms may seem illogically named, but the first of these two terms serves the purpose of diffusing the face Mach number in the case of low Mach number flow and pressure differences in neighboring cells. Notice how this term falls away for large Mach numbers. The second term diffuses the face pressure due to velocity difference between the cells to the right and left of the cell face ($u_R - u_L$). For supersonic flows the term $\mathcal{P}_{(5)}^+(M_L)\mathcal{P}_{(5)}^-(M_R) = 0$, if M_L and M_R have the same sign, and so $p_u = 0$.

3.6 Lax-Friedrichs scheme

The Lax-Friedrichs scheme, as well as the First Ordered Centered (FORCE) scheme presented in Section 3.7, are not primary topics of study in this thesis. Simulations have all the same been run with the schemes for comparison purposes, and the Lax-Friedrichs flux function is thus presented in this section.

The flux of the Lax-Friedrichs scheme is

$$\mathbf{f}_{i+\frac{1}{2}}^{\text{LF}} = \frac{1}{2}(\mathbf{F}(\mathbf{U}_i) + \mathbf{F}(\mathbf{U}_{i+1})) + \frac{1}{2} \frac{\Delta x}{\Delta t} (\mathbf{U}_i - \mathbf{U}_{i+1}). \quad (3.61)$$

3.7 FORCE scheme

A brief outline of the First Ordered Centered (FORCE) centered scheme is included in this section, as simulation results obtained using this scheme have been compared to results found using AUSM schemes. In Chapter 5 results have been compared to those of BIGCCS publications that have made use of the FORCE scheme. Notice that in Chapter 5 most of the FORCE results presented are from the original articles, such as [7]. It will be explicitly stated if FORCE calculations have been run using the author's own programs. For a more thorough overview of the scheme see [32, Sec. 7.4.2].

For the FORCE scheme, the numerical flux is given as

$$\mathbf{f}_{i+\frac{1}{2}} = \frac{1}{2} \left(\mathbf{f}_{i+\frac{1}{2}}^{\text{RI}} + \frac{1}{2}(\mathbf{F}_i^n + \mathbf{F}_{i+1}^n) \right) + \frac{1}{4} \frac{\Delta x}{\Delta t} (\mathbf{U}_i^n - \mathbf{U}_{i+1}^n) \quad (3.62)$$

The flux function $\mathbf{f}_{i+\frac{1}{2}}^{\text{RI}}$ is known as the Richtmyer flux. It is calculated using the two-step Richtmyer version of the Lax-Wendroff method [32, Sec. 5.3.4]. It is a two-step method because it creates the state $\mathbf{U}_{i+\frac{1}{2}}^{n+\frac{1}{2}}$ for which it evaluates the flux. The state created is given by

$$\mathbf{U}_{i+\frac{1}{2}}^{n+\frac{1}{2}} = \frac{1}{2} (\mathbf{U}_i^n + \mathbf{U}_{i+1}^n) + \frac{1}{2} \frac{\Delta t}{\Delta x} (\mathbf{F}_i^n - \mathbf{F}_{i+1}^n), \quad (3.63)$$

and from this the Richtmyer flux can be evaluated:

$$\mathbf{f}_{i+\frac{1}{2}}^{\text{RI}} = \mathbf{F}(\mathbf{U}_{i+\frac{1}{2}}^{n+\frac{1}{2}}). \quad (3.64)$$

As pointed out in [32, Sec. 7.4.2] it is interesting to note that the FORCE flux function is the arithmetic average of the Richtmyer flux and the flux function of the Lax-Friedrichs method. Thus the FORCE flux function can be obtained by combining the flux functions in Equations (3.61) and (3.64).

$$\mathbf{f}_{i+\frac{1}{2}} = \frac{1}{2} \left(\mathbf{f}_{i+\frac{1}{2}}^{\text{RI}} + \mathbf{f}_{i+\frac{1}{2}}^{\text{LF}} \right). \quad (3.65)$$

3.8 Boundary conditions

The need for prescribing boundary conditions (BCs) can be established based on the eigenvalues of the Jacobian of a system of PDEs. The homogeneous equilibrium model has three distinct eigenvalues, as mentioned in Section 2.3. Thus, zero to three boundary conditions must be specified at each boundary depending on the sign of the eigenvalues [21]. Often it is common to calculate characteristic boundary conditions based on primitive variables, and for a rigorous implementation this is what ought to be done.

In this work, the effect of boundary conditions is, however, not a primary concern, and thus simplified approaches such as variable extrapolation has been utilized. It is worth mentioning, that what is referred to as the *pressure BC* in [22] has been implemented for the test case presented in 5.3. This boundary condition is an outlet boundary condition that makes use of one ghost cell. The outlet pressure is set to ambient pressure, whereas velocity, mixture entropy and mixture composition are extrapolated from the interior. Based on these values all other variables are calculated.

Another utilized boundary condition is the cyclic boundary condition, for which the last cell of the domain is immediately followed by the first cell of the domain in calculations, when information is being propagated from left to right. Thus the flux leaving the last cell of the domain is equal to the flux entering the first cell.

Chapter 4

Thermodynamics

This chapter describes generally the purpose of an equation of state, and specifically outlines the Span-Wagner equation of state that has been used in all the simulations presented in this thesis.

4.1 Equation of state

Equations of state (EOSs) are a set of thermodynamic relations between two or more state variables. Such equations are needed as closure conditions for a number of flow models, including the homogeneous equilibrium model utilized in this report.

4.2 Span-Wagner equation of state

The simulations performed in this thesis were performed using the Span-Wagner [30] equation of state. This equation of state is based on experimentally obtained thermodynamic data for CO_2 , which has been fitted to a function representing the residual part of the Helmholtz free energy. The Span-Wagner EOS library used as well as corresponding subroutines were provided by SINTEF Energy Research.

The Span-Wagner EOS has an estimated uncertainty of up to ± 0.05 % in density, ± 1.00 % in speed of sound and $\pm 1.5\%$ in isobaric heat capacity [30]. For details on the development of the algorithm used to find other variables from density and internal energy in single and two-phase regions above the triple point, see [6].

The Span-Wagner EOS does not include the solution of phase composition at the triple point or at properties at the sublimation line. Using the library provided by SINTEF, such calculations are still possible due to the implementation of several additional functions. At the triple point, the properties are calculated using the Clapeyron equation. For details on the development of these additional functions, see [7].

The algorithms for calculating the primitive variables from the conserved variables were included in the Span-Wagner library provided by SINTEF Energy Research. For details on the calculation of these see Section 4.2.1.

4.2.1 Calculating primitive variables

As a new time step is calculated according to one of the methods in Section 3.4, the vector \mathbf{U} of conserved variables is obtained for the new time step and from this the primitive variables must be calculated. Since for HEM, as can be seen in Equation 2.7, the vector \mathbf{U} consists of

$$\mathbf{U} = \begin{bmatrix} \rho \\ \rho v \\ \rho E, \end{bmatrix} \quad (4.1)$$

it is clear that the mixture density, ρ , the total specific energy, E , and also the velocity, v , is readily available. Hence it is also simple to calculate the internal energy, e , as can be seen from Equation (2.6). Thus, at every time step the only two known state variables are the density and internal energy, and from these two variables all other variables must be calculated.

The algorithm for solving for the primitive variables is an iterative procedure that could require looking for the right solution in different phases. In practice, the solution is first sought in the phase that the cell contained in the previous time step. The algorithm for solving for the primitive variables is presented in [7], and here the problem of calculating the temperature, pressure and mass fractions from the density and internal energy is called the ρu -problem, since one seeks to extract the primitive variables from the mixture density and the internal energy, here denoted by the letter u .

4.2.2 Calculating variables from entropy, s , and pressure, p

As explained in Section 3.8, the so-called *pressure BC*, an outlet boundary condition, sets the pressure, p , on the boundary and extrapolates the entropy, s , from the interior. Similarly, as explained in Section 3.3, when MUSCL-reconstruction was utilized in the present work, either the conserved variables or pressure, entropy and velocity were chosen as the variables to be reconstructed. Thus, for these two purposes it is necessary to be able to calculate the temperature, as well as phasic densities and volume fractions based on the pressure and entropy. An algorithm for this is also presented in [7], where the problem is called the Ps -problem. Pressure is here denoted by the uppercase P .

Chapter 5

Results and discussion

Chapter 5 describes the test cases simulated in this thesis work and presents the results obtained from these simulations. Three main test simulations have been performed: advection of a gas fraction curve in liquid, a shock tube problem with liquid, gaseous and solid CO₂ occurring and the depressurization of a pipe containing liquid CO₂. The two latter cases were taken from [7], where the homogeneous equilibrium model was used in combination with the FORCE scheme and the Span-Wagner EOS. Thus these simulations provide a point of reference for the AUSM simulations performed, since the numerical flux function is what separates these simulations, along with different boundary conditions.

5.1 Simple advection in a 12 m tube

The simple advection of a gas fraction in liquid, in the shape of a Gauss-curve, was simulated. This test case used the same parameters found in [23], where the multi-stage predictor-corrector scheme [31][33], MUSTA, was studied. Results are not directly comparable, as the the simulation in [23] was performed with a six-equation model.

It is of key interest to see how a numerical scheme handles advection in a tube with no source terms, and pressure, temperature and velocity kept constant. Results obtained are of interest even without comparing them to other simulations, as the ideal result is easily predicted — namely a perfectly similar curve advected to a given distance based on the velocity and the period the simulation was run for.

The Gauss-curves was advected at constant velocity 100 m/s for a period of 0.03 s. The simulation was run with various AUSM-family schemes, as well as FORCE and Lax-Friedrichs. All simulations were run with a CFL-number of 0.5 with a cyclic boundary condition.

The formula for the gas fraction Gauss curve is

$$\alpha_g = (a - 2\epsilon) \exp\left(-\frac{(x - b)^2}{2\mathcal{L}^2}\right) + \epsilon. \quad (5.1)$$

Here, $a - 2\epsilon$, is the height of the curve's peak. b is the location of the curve's peak and \mathcal{C} is the standard deviation - which determines the width of the curve.

The curve's initial position was around the point $b = 6$ m. The solutions for various grid sizes have been compared to the exact solution, which is the same Gauss-curve that was the initial condition only centered around $x = 9$ m. The height of the peak of the initial curve is $a - 2\epsilon = 1 - 2 \times 10^{-6}$ and $\mathcal{C} = 0.42$ m. The parameter $\epsilon = 1 \times 10^{-6}$ ensures that there is a small amount of gas in the area outside the Gauss-curve, where the remaining volume is of the liquid phase.

The test case was simulated using first order accurate AUSM^+ , as well as MUSCL reconstructed AUSM^+ . For the latter case, two different sets of reconstructed variables were considered, namely the conserved variables, and pressure, velocity and entropy. Two different limiters were considered, the minmod-limiter and the van Leer-limiter.

The test case was also simulated using AUSM^+ -up as well as MUSCL- AUSM^+ -up with the minmod-limiter employed and conserved variables reconstructed. Further, the test case was run with the Lax-Friedrichs scheme and using MUSCL-FORCE.

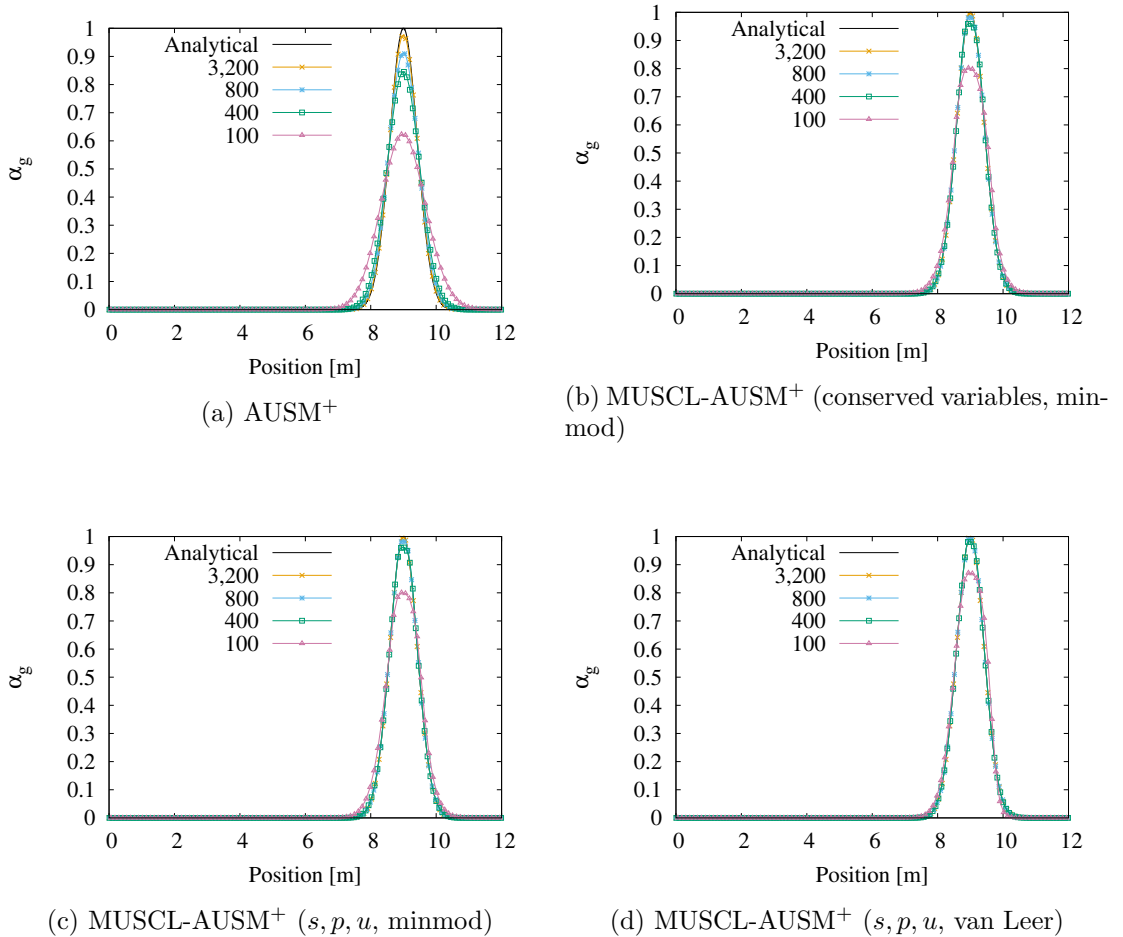


Figure 5.1: Grid refinement of advected Gauss curve in 12 m tube. AUSM^+ .

Figure 5.1 shows the effect of grid refinement on the advected curve. It can be seen from the Figure that the first order result in Figure 5.1a has the slowest convergence, whereas MUSCL reconstruction with the van Leer-limiter has the fastest convergence. These results are confirmed in Tables 5.1, 5.2, 5.3 and 5.4. Here, $\mathcal{E}(\alpha_g)$ denotes the error of the gas volume fraction, α_g .

From Table 5.1 it can be seen that first order AUSM⁺ has a convergence rate approaching unity, as expected. Further, Tables 5.2 and 5.3 show that MUSCL reconstruction of the conserved variables gives a higher convergence rate – approaching two, as expected – than does reconstruction of entropy, pressure and velocity. The calculated one-norm error is lower for reconstruction of the conserved variables for the five finest grids.

Both sets of reconstructed variables in Tables 5.2 and 5.3 give convergence rates of above 1.90 as expected for a scheme that makes use of linear MUSCL reconstruction. As explained in Section 3.3, for extrema and when gradients are zero, the first-order scheme is regained. Hence it is expected to get convergence rates approaching a rate of 2.0, since the numerical scheme will be up to second order accurate.

As can be seen from Table 5.4, employing the Van Leer limiter gives more accurate results and higher convergence rates than the minmod limiter. This limiter is thus more effective for this test problem.

Table 5.1: 1-norm error and convergence rate for advected gas volume fraction in 12 m tube. AUSM⁺.

Δx [m]	$\ \mathcal{E}(\alpha_g)\ _1$	Conv. rate
0.12	4.67×10^{-1}	-
0.06	2.94×10^{-1}	0.67
0.03	1.70×10^{-1}	0.79
0.015	9.29×10^{-2}	0.87
0.0075	4.88×10^{-2}	0.93
0.00375	2.50×10^{-2}	0.96
0.001875	1.27×10^{-2}	0.98
0.0009375	6.38×10^{-3}	0.99

Table 5.2: 1-norm error and convergence rate for advected gas volume fraction in 12 m tube. MUSCL-AUSM⁺ (conserved variables, minmod-limiter).

Δx [m]	$\ \mathcal{E}(\alpha_g)\ _1$	Conv. rate
0.12	1.69×10^{-1}	-
0.06	5.51×10^{-2}	1.62
0.03	1.99×10^{-2}	1.47
0.015	5.74×10^{-3}	1.79
0.0075	1.59×10^{-3}	1.85
0.00375	4.26×10^{-4}	1.90
0.001875	1.14×10^{-4}	1.90
0.0009375	2.98×10^{-5}	1.93

Table 5.3: 1-norm error and convergence rate for advected gas volume fraction in 12 m tube. MUSCL-AUSM⁺ (s, p, u , minmod-limiter).

Δx [m]	$\ \mathcal{E}(\alpha_g)\ _1$	Conv. rate
0.12	1.76×10^{-1}	-
0.06	5.75×10^{-2}	1.61
0.03	1.76×10^{-2}	1.71
0.015	6.13×10^{-3}	1.52
0.0075	1.76×10^{-3}	1.80
0.00375	4.84×10^{-4}	1.86
0.001875	1.28×10^{-4}	1.92
0.0009375	3.38×10^{-5}	1.92

Table 5.4: 1-norm error and convergence rate for advected gas volume fraction in 12 m tube. MUSCL-AUSM⁺ (s, p, u , Van Leer-limiter).

Δx [m]	$\ \mathcal{E}(\alpha_g)\ _1$	Conv. rate
0.12	1.20×10^{-1}	-
0.06	3.75×10^{-2}	1.68
0.03	9.90×10^{-3}	1.92
0.015	2.76×10^{-3}	1.84
0.0075	7.36×10^{-4}	1.91
0.00375	1.88×10^{-4}	1.97
0.001875	4.73×10^{-5}	1.99
0.0009375	1.20×10^{-5}	1.98

Figure 5.2 shows the result of first-order and MUSCL reconstructed AUSM⁺-up using conserved variables. Notice when comparing Tables 5.1 and 5.2 to 5.5 and 5.6 that the convergence rates are exactly the same for the first order and the MUSCL cases respectively, regardless of whether AUSM or AUSM⁺-up was utilized. The reason for this can be observed in Equations (3.47) and (3.48). Both the velocity diffusion term p_u and the pressure diffusion term M_p fall away when there is constant pressure and velocity, thus one regains AUSM⁺.

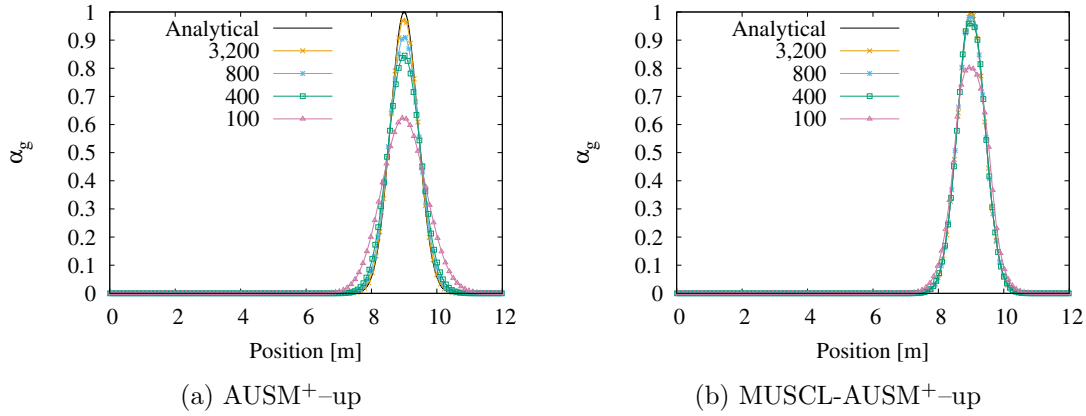


Figure 5.2: Grid refinement of advected Gauss curve in 12 m tube. AUSM⁺-up.

Table 5.5: 1-norm error and convergence rate for advected gas volume fraction in 12 m tube. AUSM⁺-up.

Δx [m]	$\ \mathcal{E}(\alpha_g)\ _1$	Conv. rate
0.12	4.67×10^{-1}	-
0.06	2.94×10^{-1}	0.67
0.03	1.70×10^{-1}	0.79
0.015	9.29×10^{-2}	0.87
0.0075	4.88×10^{-2}	0.93
0.00375	2.50×10^{-2}	0.96
0.001875	1.27×10^{-2}	0.98
0.0009375	6.38×10^{-3}	0.99

Table 5.6: 1-norm error and convergence rate for advected gas volume fraction in 12 m tube. MUSCL-AUSM⁺-up.

Δx [m]	$\ \mathcal{E}(\alpha_g)\ _1$	Conv. rate
0.12	1.69×10^{-1}	-
0.06	5.51×10^{-2}	1.62
0.03	1.99×10^{-2}	1.47
0.015	5.74×10^{-3}	1.79
0.0075	1.59×10^{-3}	1.85
0.00375	4.26×10^{-4}	1.90
0.001875	1.14×10^{-4}	1.90
0.0009375	2.98×10^{-5}	1.93

Figure 5.3 shows the gas volume fraction after 0.03 seconds calculated using first-order accurate Lax-Friedrichs. It is clear when comparing Figure 5.3 to Figure 5.1a that

a scheme such as Lax-Friedrichs is significantly more diffusive than AUSM⁺. Table 5.7, showing the one-norm error and convergence rate for the Lax-Friedrichs scheme, confirms this. It is clear that LF would require significantly finer grids to achieve the same accuracy as AUSM⁺. Such a result is expected, as Lax-Friedrichs is known to be a highly diffusive scheme.

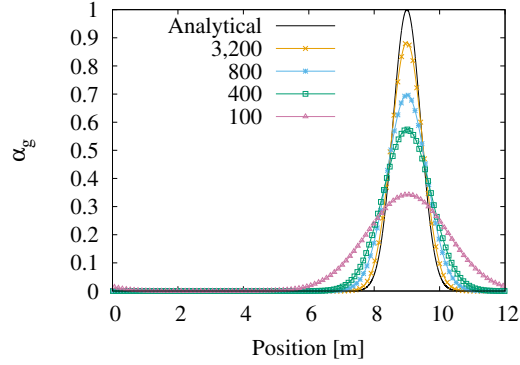


Figure 5.3: Grid refinement of advected Gauss curve in 12m tube. Lax-Friedrichs.

Table 5.7: 1-norm error and convergence rate for advected gas volume fraction in 12m tube. Lax-Friedrichs.

Δx [m]	$\ \mathcal{E}(\alpha_g)\ _1$	Conv. rate
0.12	9.92×10^{-1}	-
0.06	7.69×10^{-1}	0.37
0.03	5.51×10^{-1}	0.48
0.015	3.64×10^{-1}	0.60
0.0075	2.22×10^{-1}	0.71
0.00375	1.26×10^{-1}	0.81
0.001875	6.80×10^{-2}	0.89

Figure 5.4 shows the effect of grid refinement on the solution calculated using MUSCL-FORCE with the minmod-limiter employed. The corresponding 1-norm error and convergence rate can be seen in Table 5.8. It is clear that the calculated one-norm error is smaller for AUSM⁺ – compare Tables 5.8 and 5.2 – for all corresponding grid sizes, and the calculated convergence rate is lower for MUSCL-FORCE. It is reasonable that such a result should be obtained, due to the upwinding nature of AUSM schemes. FORCE on the other hand is a centered scheme, and thus for an advection test case like this, AUSM⁺ has an advantage over FORCE.

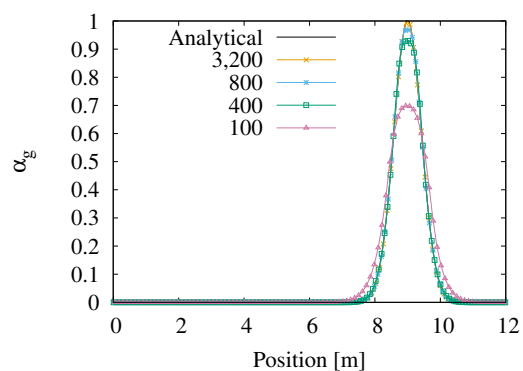


Figure 5.4: Grid refinement of advected Gauss curve in 12 m tube. MUSCL-FORCE.

Table 5.8: 1-norm error and convergence rate for advected gas volume fraction in 12 m tube. MUSCL-FORCE.

Δx [m]	$\ \mathcal{E}(\alpha_g)\ _1$	Conv. rate
0.12	3.05×10^{-1}	-
0.06	1.16×10^{-1}	1.40
0.03	3.78×10^{-2}	1.62
0.015	1.34×10^{-2}	1.50
0.0075	3.74×10^{-3}	1.84
0.00375	1.01×10^{-3}	1.88
0.001875	2.76×10^{-4}	1.88

5.2 Shock tube

In order to test and compare the AUSM-schemes' ability to deal with a shock tube problem where three phases are known to occur, the shock tube problem described in [7] was simulated. This allows for comparing the performance of AUSM to the FORCE scheme used originally.

The initial conditions in the shock tube are presented in Table 5.9. The simulations were run with AUSM⁺-up using MUSCL with the minmod-limiter employed. The MUSCL-reconstructed variables were the conserved variables ρ , ρu and ρE . Similar to the case in the original article, the simulations were run until $t = 0.06$ s using the second-order accurate strong-stability-preserving (SSP) Runge-Kutta (RK) method. The pipe was set to be 100 m, with a uniform temperature and a pressure discontinuity in the middle of the pipe as initial conditions, see Table 5.9.

The effect of grid refinement of the solution can be seen in Figure 5.5, whereas a comparison with the obtained results in [7] can be seen in Figure 5.6. These results were found using MUSCL-FORCE. The original data from [7] provided by SINTEF Energy Research were used to make the plots in Figure 5.6.

Table 5.9: Initial conditions for shock tube test.

Variable	Left side	Right side
Pressure	3 MPa	0.1 MPa
Velocity	0 m/s	0 m/s
Temperature	250 K	250 K

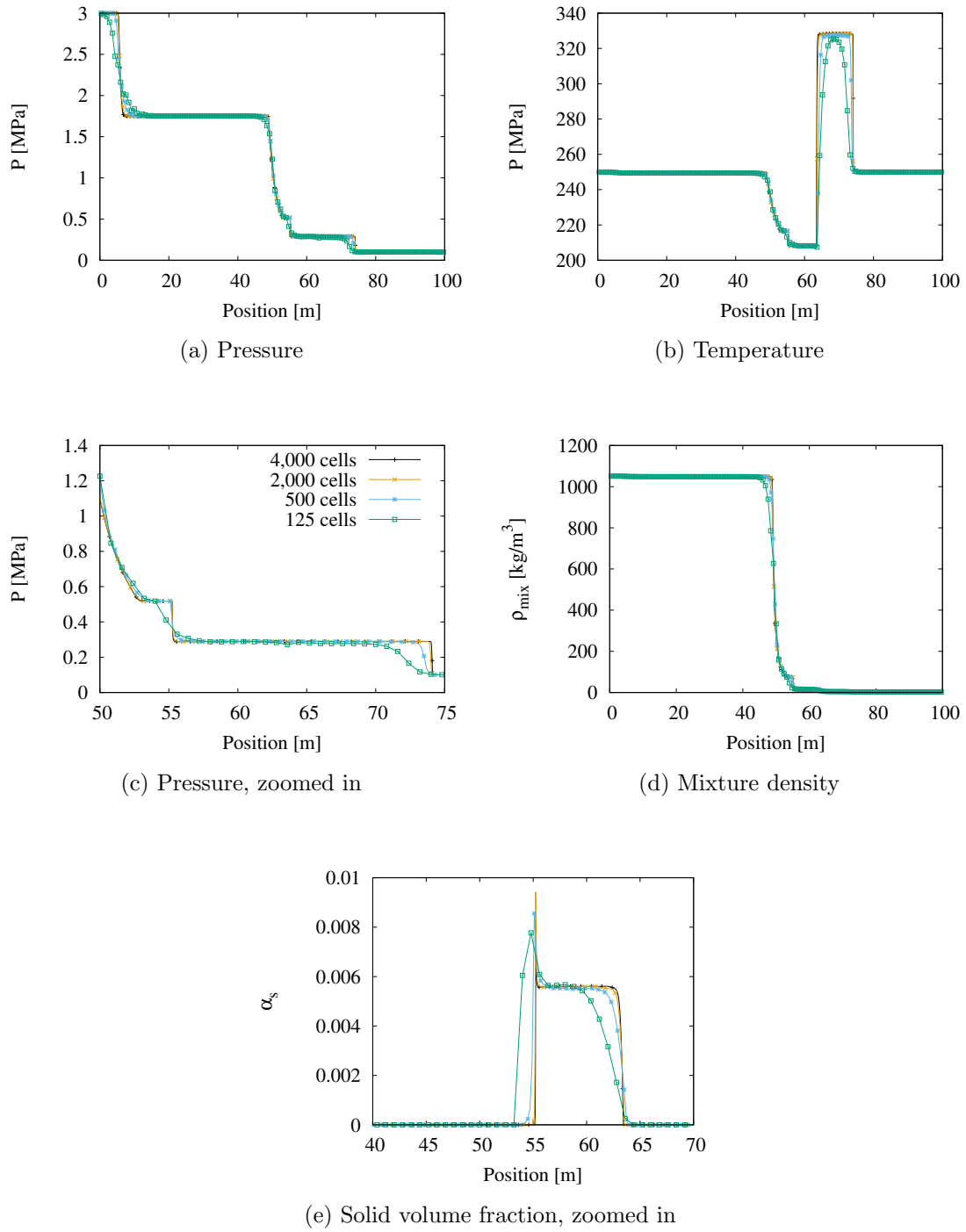


Figure 5.5: Shock tube problem solved with MUSCL-AUSM⁺-up, effect of grid refinement.

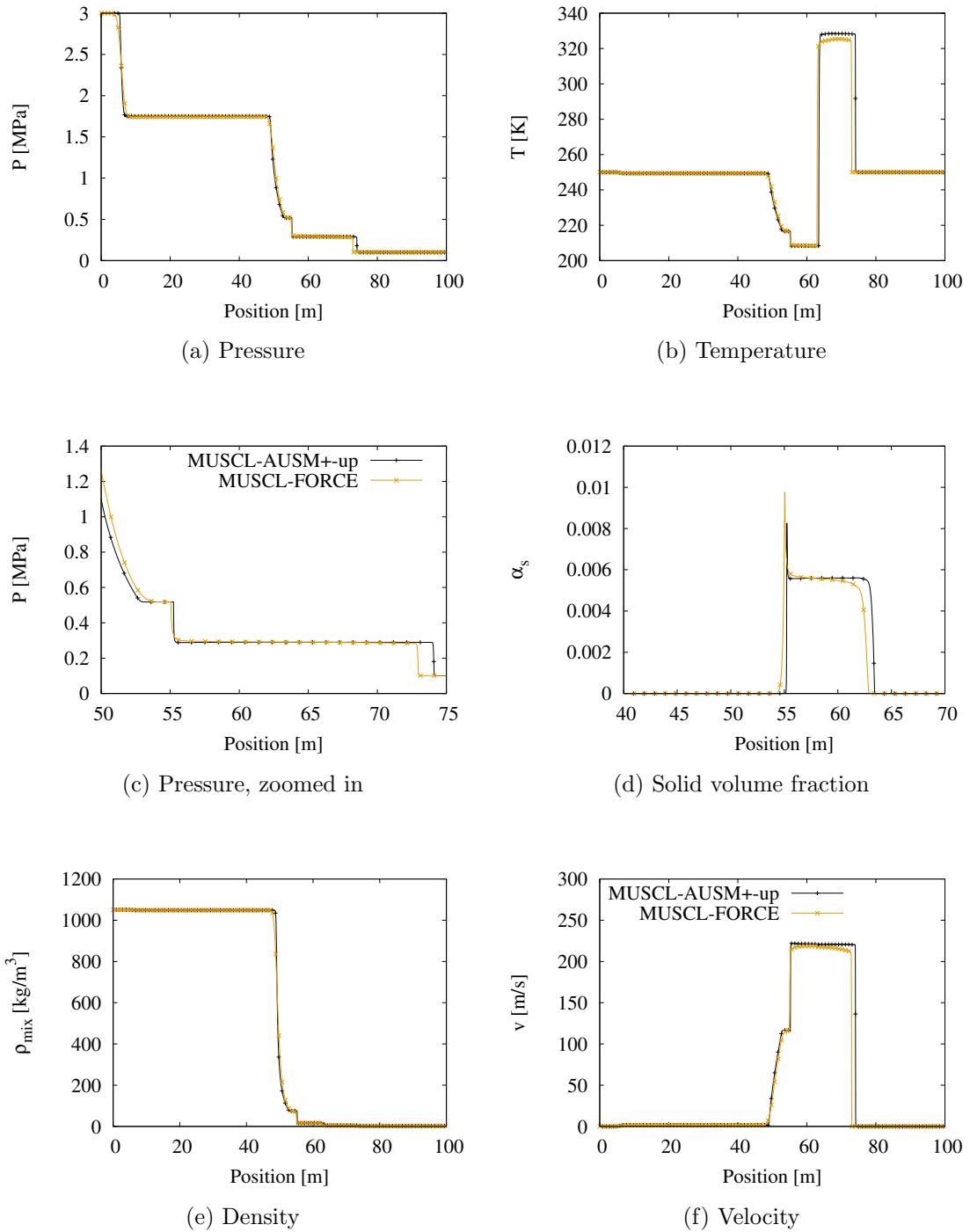


Figure 5.6: Shock tube, comparison of MUSCL-AUSM⁺–up and MUSCL-FORCE, 4,000 cells.

MUSCL-AUSM⁺–up is able to successfully simulate the case. Figure 5.6d shows that there is a small solid volume fraction present. As pointed out in [7], one can see a pressure plateau for the saturation pressure value of approximately 1.75 MPa, a plateau

for the triple point pressure of 0.518 MPa and a plateau for the sublimation pressure of approximately 0.3 MPa.

Comparing the results of MUSCL-AUSM⁺-up and MUSCL-FORCE, reveals certain differences especially in the right half of the pipe. Information is propagated faster in the right half of the pipe with AUSM compared to what is the case with FORCE. Notice the shock discontinuity location in Figure 5.6c.

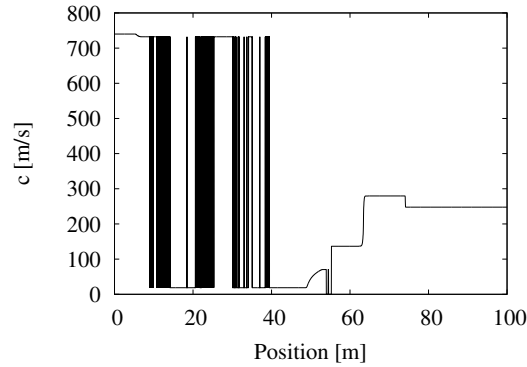
AUSM⁺ predicts a higher maximum temperature than does FORCE – (327.3 K vs 325.1 K). This is due to a higher velocity obtained in the right side of the pipe using AUSM⁺-up. It is likely that either or both of the above-mentioned schemes are not fully converged, and that this is the reason why one is experiencing such differences.

The simulation of this shock tube test case is a computationally intensive simulation, and to compute fine enough grids to prove convergence and hence that the schemes are consistent could take weeks. Such fine-grid simulations have for this reason not been performed.

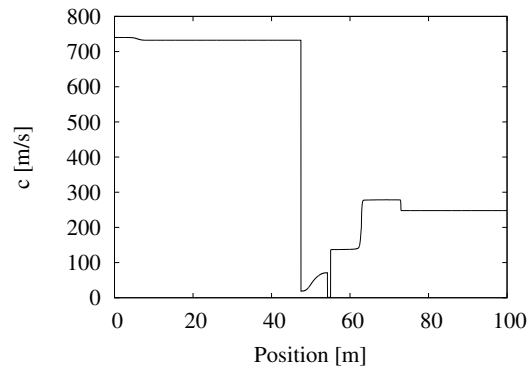
Since it is for the momentum equation part of the numerical flux that the AUSM flux splitting applies (see Equation (3.27)), this could also explain why this is where there is a significant difference between AUSM⁺-up and FORCE for several of the variables. The different evaluation of this flux could cause the evaluation of the velocity to be affected, and hence also the calculation of internal energy and temperature. It is also possible that the result obtained using AUSM⁺-up simply is more accurate as the scheme is less diffusive and appears to give a better resolution of the edges of the rarefaction waves seen in Figures 5.6a and 5.6c.

5.2.1 Speed of sound problems with AUSM schemes

Plots of the speed of sound for MUSCL-AUSM⁺-up and MUSCL-FORCE can be seen in Figure 5.7.



(a) MUSCL-AUSM⁺-up



(b) MUSCL-FORCE

Figure 5.7: Shock tube, comparison of speed of sound, MUSCL-AUSM⁺-up and MUSCL-FORCE, 4,000 cells.

Figure 5.7a shows the evaluated speed of sound after 0.06 s for MUSCL-AUSM⁺-up. Notice the unexpected oscillations in speed of sound in the left part of the pipe. AUSM-schemes separate the flux of convective terms and pressure terms. This separation of the numerical flux function results in certain parts of the fluid in the oscillating area to be evaluated as pure liquid and other parts to be evaluated as liquid with a small amount of gas present.

The oscillations occurring are thus due to the different phase evaluations, and the discontinuity in speed of sound that one sees when moving from liquid to liquid-vapor. The reason for this is described in Section 2.3.1.

In the present test case, there is only a fraction vapor present at certain points in the left part of the pipe, but this causes the speed of sound to drop from 732.2 m/s to 18.7 m/s.

As can be seen in Section 3.5 the value of the Mach number and hence the value for the

speed of sound is key for the formulation of the convective flux and the pressure flux, for all AUSM schemes. Although the speed of sound falls away for the convective flux in the AUSM family of schemes, as can be seen in Equation (3.30), the dissipation term, M_p , see Equation (3.47), becomes zero for large Mach numbers in AUSM⁺-up. Hence this term depends greatly on the speed of sound.

The choice of pressure and Mach number splitting is also determined based upon whether the flow is supersonic, and the pressure flux is affected by the Mach number directly for subsonic flows (see Equation (3.48)).

The effect of the oscillating speed of sound on the flux function is complex, but it is clear that the dissipation terms will not function as intended and that such frequent oscillations are far from ideal. However, the results presented where such oscillations have taken place, are reasonable when compared to MUSCL-FORCE.

An obvious solution to this problem is to use a different flow model or a different numerical flux function. As can be seen in Figure 5.7b, MUSCL-FORCE does not experience any such oscillations. Thus it seems clear that for this combination of thermodynamic solver and flow model, it is preferable to use FORCE over AUSM⁺-up.

5.2.2 Parameter tuning problems with AUSM schemes

Several challenges arose when attempting to solve the shock tube problem with AUSM schemes. AUSM⁺ failed to capture the physics of the test case correctly for the default values of β and ζ , presented in Equations (3.41) and (3.42), causing the expansion wave seen at $x = 50$ m to remain a discontinuity. Setting $\beta = 0$, with ζ remaining set to $\zeta = \frac{3}{16}$, fixed this, but it is clearly disadvantageous that the numerical flux function is sensitive to parameter tuning in order to get a correct solution.

Another challenge that presented itself when performing simulations with AUSM⁺-up was determining the the cut-off Mach number. This number is a problem-specific parameter that provides dissipation at low Mach numbers. As can be seen from Equation (3.47), the dissipation term increases in magnitude as the value of the scaling function f_c decreases. Thus, as can be seen from Equation (3.46), setting a low cut-off Mach number will cause significant dissipation in regions with low Mach numbers. Contrariwise setting a low cut-off Mach number will limit the dissipation of the pressure flux in Equation (3.48).

As mentioned in Section 3.5.2, [24] suggests setting the cut-off Mach number to $M_{co} = 10^{-4}$. The idea is that for cases without an obvious free-stream Mach number, the cut-off Mach number should be a very small, non-zero number. Simulations were run with this parameter set to 10^{-4} , but the results gave significant oscillations and an unstable solution. For this reason, as suggested in [26] for unsteady problems, the cut-off Mach number was instead set to 1.0.

The need for parameter tuning in AUSM⁺-up is disadvantageous, and different approaches have been taken in order to improve AUSM schemes and the problems related to problem-specific tuning of parameters. These range from the development of new parameter-tuning techniques for use with AUSM⁺-up [26] to the development of a new numerical flux function called Simple Low-dissipation AUSM (SLAU) [28] that does not require a cut-off Mach number to be specified. Further information on recent developments of AUSM schemes for multiphase flow simulations may also be found in [12].

5.3 Depressurization of pipe

The depressurization test case specified in [7] was run using AUSM⁺-up as well as FORCE for comparison purposes. The test case describes a 100 m long pipe filled with liquid CO₂, initially at a pressure of 10 MPa and a temperature of 300 K. The right side of the pipe is opened to atmospheric conditions at $t = 0$. The boundary condition referred to as the *pressure BC* in [22] and described in Section 3.8 was used as the BC for the outlet in this simulation.

The case describes a scenario where a pipe is opened to atmospheric conditions, causing the pressure to drop as an expansion wave travels from the opening to the interior of the pipe. Because of the lowered pressure, some of the liquid will turn into gas, and eventually solid will also form in the pipe. This can be seen in Figures 5.8 and 5.10 which show the results at times 0.2 s and 7.4 s respectively, the same times as figures in [7] show results for.

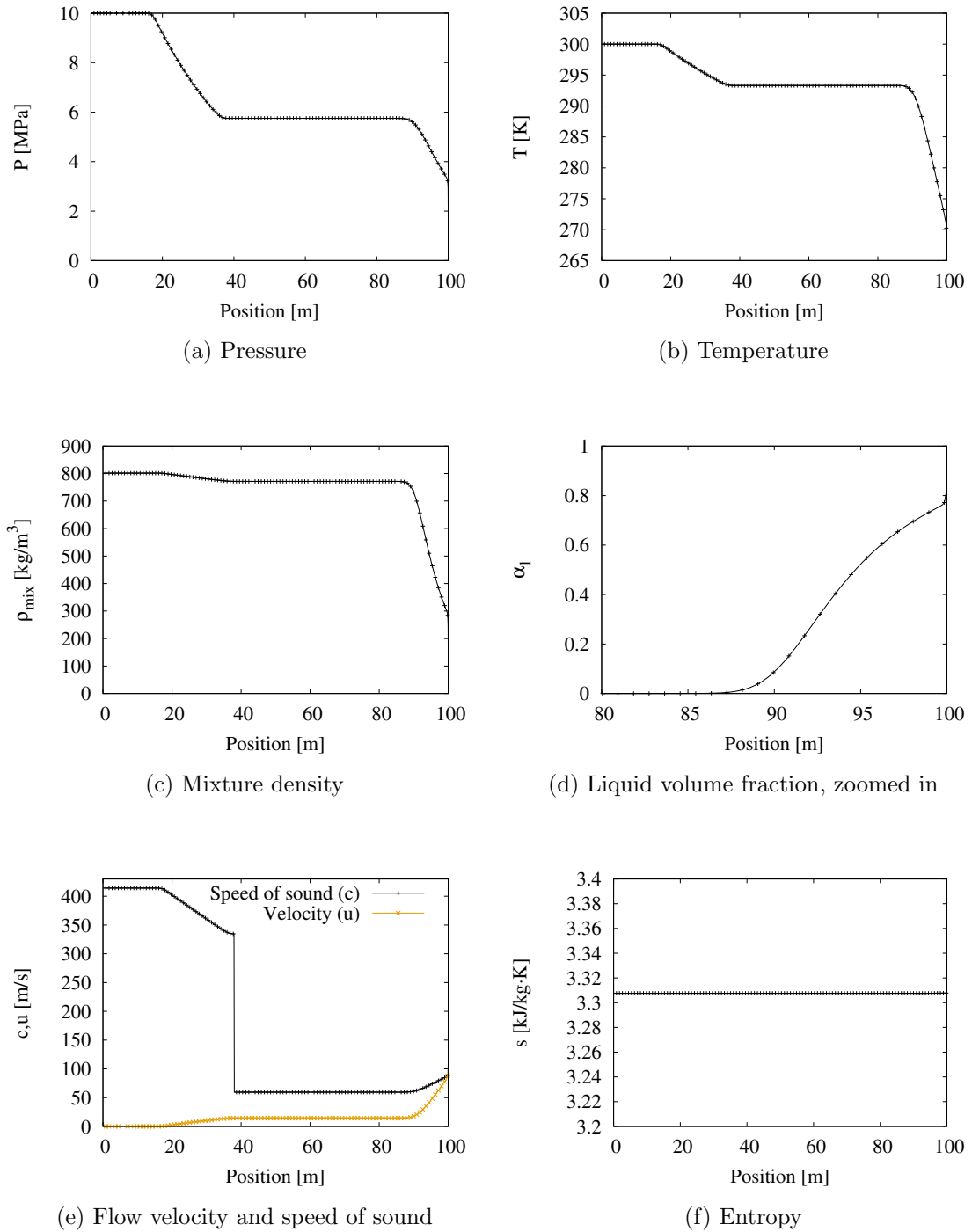


Figure 5.8: Depressurization of pipe solved with AUSM⁺-up, 1,000 cells.
 $t = 0.2$ s.

Figure 5.8e shows the velocity as well as the speed of sound in the pipe at 0.2 s. Notice that the results are here calculated using first-order AUSM⁺-up. Figure 5.8e shows that the outlet is choked since at the outlet the velocity and speed of sound are the

same.

In the region from 40 m to 90 m the speed of sound is less than 100 m/s, since the phase is liquid-vapor in Figure 5.8e. However, the speed of sound in this region is over 300 m/s when calculated with MUSCL-FORCE [22], because the region is evaluated to be pure liquid. When calculating the speed of sound with MUSCL-AUSM⁺-up the speed of sound oscillates in this region, similarly to what was described in Section 5.2. The speed of sound calculated with MUSCL-FORCE and MUSCL-AUSM⁺-up can be seen in Figure 5.9f.

Similar to what was pointed out in Section 5.2, it is a major disadvantage for AUSM⁺-up that for HEM the discontinuity in the evaluated speed of sound, see Section 5.2, causes these oscillations when combined with this numerical flux function.

With the exception of the speed of sound, the simulations show good correspondence with the results obtained with the MUSCL-FORCE simulations. MUSCL-AUSM⁺ is less diffusive than MUSCL-FORCE as can be seen from the sharper edges of the expansion waves in Figure 5.9a.

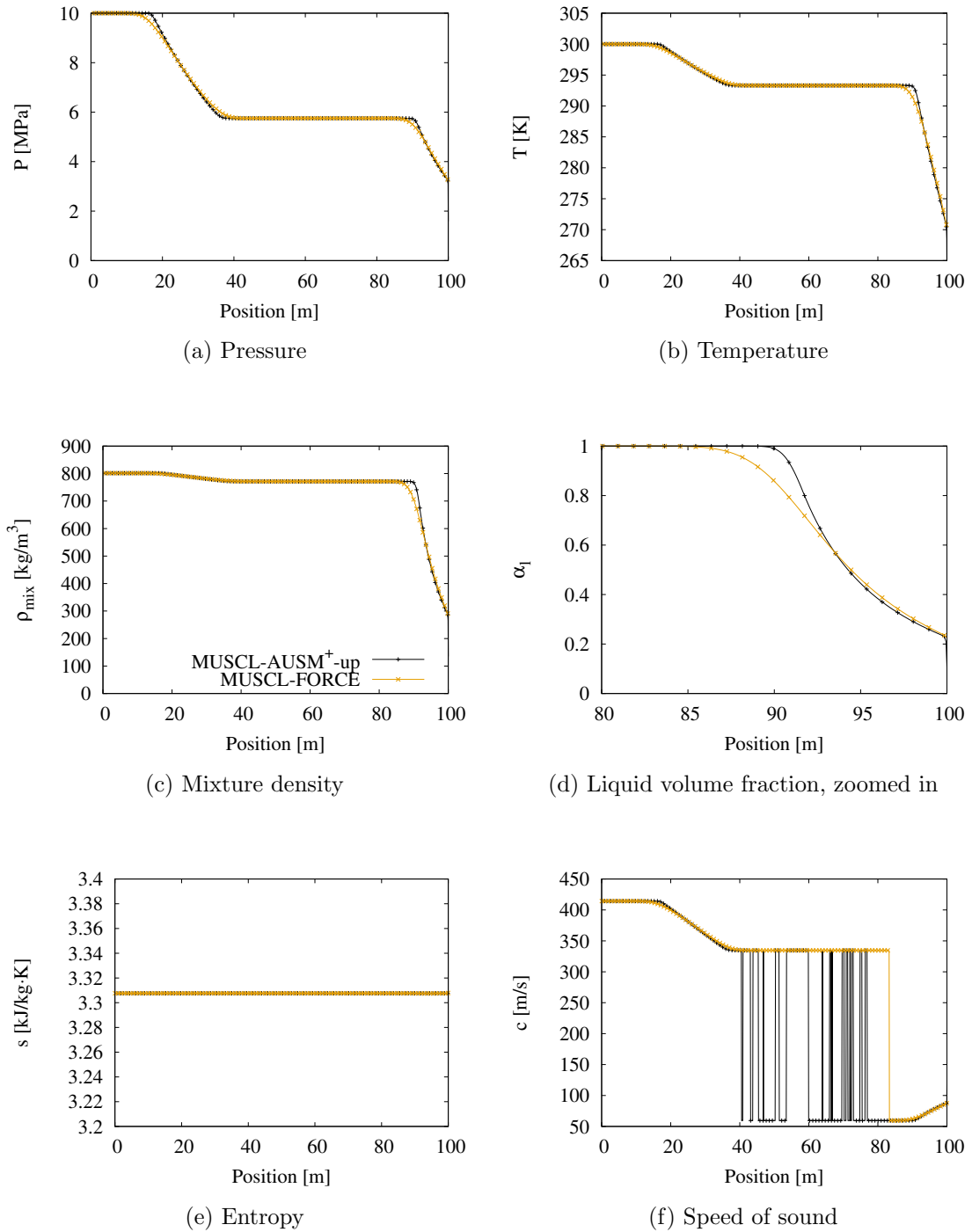


Figure 5.9: Comparison of depressurization case, solved with MUSCL-AUSM⁺-up and MUSCL-FORCE, 1,000 cells. $t = 0.2$ s.

Figure 5.10 shows the simulation run until 7.4 s. The MUSCL-AUSM⁺-up results correspond well with the MUSCL-FORCE results, even if the minimum point that is visible at 80 m for MUSCL-AUSM⁺-up for all the variables in Figure 5.10 is not perfectly aligned

with the results from MUSCL-FORCE. Similar to what was described in Section 5.2 this could be due to the solution not being converged, or due to the numerical flux function and the way it is split in AUSM⁺-up. It could also be due to the implementation of the boundary condition, as the boundary condition implemented MUSCL-AUSM⁺-up is a simpler boundary condition than what was implemented in [7].

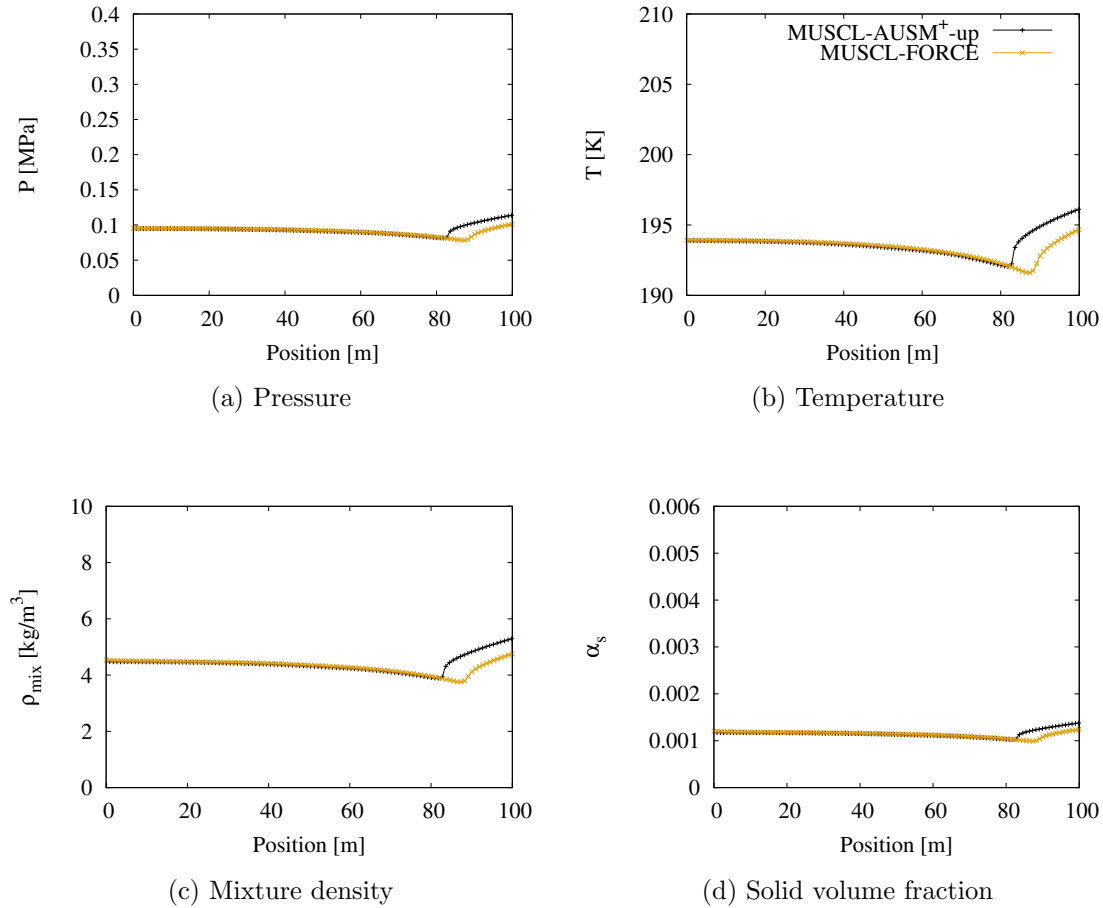


Figure 5.10: Depressurization of pipe, MUSCL-AUSM⁺-up compared to MUSCL-FORCE, 1,000 cells. $t = 7.4$ s.

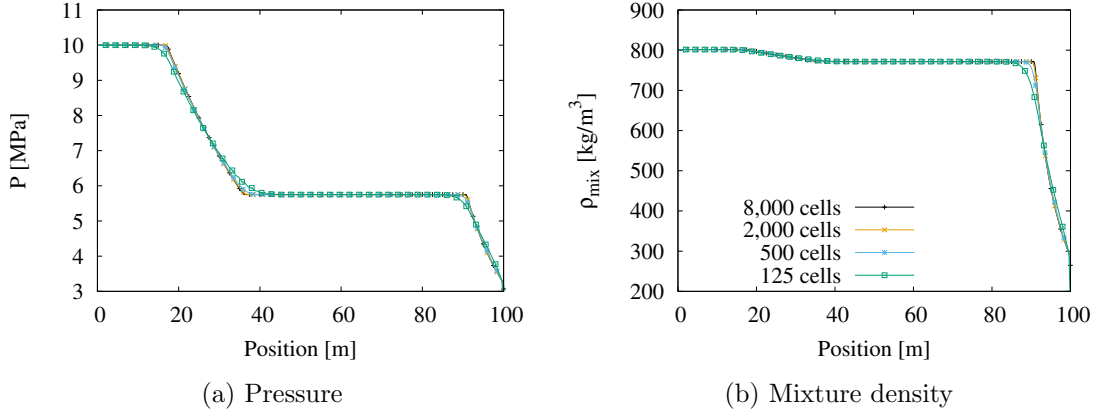


Figure 5.11: Depressurization of pipe solved with MUSCL-AUSM⁺-up, 1,000 cells. $t = 0.2$ s. Effect of grid refinement.

Table 5.10 shows the runtimes, for different grid sizes, for the depressurization case run with AUSM⁺-up and FORCE. The effect of refining the grid for MUSCL-AUSM⁺-up can be seen in Figure 5.11. Notice that these and only these FORCE-simulations presented in Table 5.10 were performed by the author. The simulations were performed with similar boundary conditions as for the runs of AUSM⁺-up, which are different from the boundary conditions used in [7].

When choosing a numerical flux function, the aim will always be to get the most accurate solution at the lowest computational costs, not just to reduce computational times themselves. For this reason, comparing the computational times is more useful when the error and convergence rates can be calculated based on an exact solution or well-established methods. Such a comparison could therefore have been performed for the advection case presented in Section 5.1. The simulations presented in Section 5.1 were however run in parallel on multiple computers, since the computation times were several days for the finest grids presented. Thus the computational times would not have been comparable.

The comparison presented in Table 5.10 aims therefore only to give a brief glimpse into the computational costs connected with the two schemes. It is clear that AUSM⁺-up is more expensive, which suggests that FORCE is a more attractive scheme when one aims to reduce computational costs. It is especially interesting to see the significant difference between MUSCL-AUSM⁺-up and MUSCL-FORCE.

One reason for the additional computing time required for AUSM⁺-up could be the different phases (liquid and liquid-vapor) occurring in the region of oscillating speed of sound seen in Figure 5.9f. Solving for the primitive variables could require extra computational time due to the thermodynamic solver looking for the solution in the liquid phase region instead of the liquid-vapor region - or vice versa. Running the program with the GNU profiling tool, *gprof*, indicated that the big differences in computational time were due to increased time spent in the thermodynamic solver routines. For this reason it could be interesting to investigate the computational times for a test case that did not have such regions of two different evaluated phases.

The increased computational time experienced with AUSM⁺-up compared to FORCE could also be considered to be worthwhile. Examining the expansion wave in Figure 5.9 shows that MUSCL-AUSM⁺-up gives better resolution of the edges of the expansion wave, and thus just over twice the computational time could mean a valuable increase in accuracy.

Table 5.10: Run-times for depressurization test case. Run until $t = 0.2$ s.

Δx [m]	Run times [s]			
	AUSM ⁺ -up	FORCE	MUSCL-AUSM ⁺ -up	MUSCL-FORCE
0.096	5.58	10.85	36.28	34.85
0.048	31.92	37.03	142.4	111.2
0.024	113.7	137.8	488.0	377.4
0.012	394.0	456.1	1,994	1,895
0.006	1,786	1,622	8,244	7,423
0.003	7,017	6,792	33,800	23,354
0.0015	26,107	25,236	137,536	69,686
0.00075	82,752	76,024	553,686	250,640

Chapter 6

Conclusions and further work

Numerical flux functions $AUSM^+$ and $AUSM^{+up}$ have been implemented for the homogeneous equilibrium model (HEM), and multiphase CO_2 test problems have been solved with real CO_2 thermodynamics using the Span-Wagner equation of state. The obtained results have been compared to results provided by SINTEF for two of the test problems solved, where the FORCE numerical flux function was utilized. For a third test case, AUSM schemes were compared to the author's own implementation of the Lax-Friedrichs and FORCE schemes.

$AUSM^+$ simulated the advection of a gas fraction profile in liquid at constant velocity and pressure with better accuracy and higher convergence rates than both Lax-Friedrichs and FORCE. For this problem, MUSCL reconstruction was utilized. Two sets of variables were reconstructed, the conserved variables, as well as density, entropy and pressure. The former gave more accurate results when used with $AUSM^+$. Two different slope limiters were utilized, the minmod limiter and the Van Leer limiter. The latter gave the highest convergence rates.

A shock tube problem was simulated. $AUSM^{+up}$ successfully produced a solution with all the expected solution features present, and a result corresponding to that calculated using FORCE (data provided by SINTEF) was obtained, with minor differences. The shock location was different, and so were the evaluated velocity and temperature. The fact that the solutions were not run until grid-independent could explain why such differences could be observed. The reason for the differently evaluated variables could also simply be due to the flux splitting nature of $AUSM^{+up}$, and simply that $AUSM^{+up}$ gives a more accurate result.

Further, for the shock tube problem $AUSM^{+up}$ only successfully simulated the problem after parameter tuning had been performed. This is a significant drawback for the scheme, when comparing with FORCE, which requires no parameter tuning.

Another significant drawback was found using AUSM schemes to solve the shock tube problem. Significant oscillations in the speed of sound could be seen in the left part of the tube. This result is due to the discontinuity that can be seen when going from pure liquid to liquid-vapor in speed of sound evaluations for HEM. In this region, the thermodynamic solver evaluated some cells to be liquid and other cells to be liquid with

as small gas fraction. Such oscillations were not seen for FORCE, and thus for a flow model like HEM, FORCE is preferable to AUSM.

The last test case run was a depressurization test case. The same speed of sound oscillations seen in the shock tube case were also observed here. AUSM⁺-up produced a satisfactory solution with all the expected solution features.

An evaluation of the computational time for AUSM⁺-up as well as FORCE was performed for this test case. This evaluation showed that FORCE gave faster run-times than AUSM⁺-up.

Future work with the AUSM family of schemes for the purpose of simulating mutliphase CO₂ should include investigations into other flow models, in order to avoid the speed of sound oscillations experienced.

Further, it would be beneficial to investigate AUSM schemes that do not require any parameter tuning in order to solve problems involving low Mach number flow. Having to specify such problem specific parameters is a significant drawback for AUSM⁺-up.

An interesting investigation would also be to examine in-depth what causes the slower runtimes for AUSM⁺-up, since the scheme used more time to evaluate a problem with the exact same flow model, setup and boundary conditions when compared to FORCE.

Bibliography

- [1] E. Aursand, P. Aursand, T. Berstad, C. Dørum, M. Hammer, S. Munkejord, and H. Nordhagen. CO₂ pipeline integrity: A coupled fluid-structure model using a reference equation of state for CO₂. *Energy Procedia*, 37:3113–3122, 2013.
- [2] P. Aursand, M. Hammer, S. T. Munkejord, and Ø. Wilhelmsen. Pipeline transport of CO₂ mixtures: Models for transient simulation. *International Journal of Greenhouse Gas Control*, 15:174–185, July 2013.
- [3] M. E. Boot-Handford, J. C. Abanades, E. J. Anthony, M. J. Blunt, S. Brandani, N. Mac Dowell, J. R. Fernández, M.-C. Ferrari, R. Gross, J. P. Hallett, et al. Carbon capture and storage update. *Energy & Environmental Science*, 7(1):130–189, 2014.
- [4] C. E. Brennen. *Fundamentals of multiphase flow*. Cambridge University Press, 2005.
- [5] T. Flåtten and H. Lund. Relaxation two-phase flow models and the subcharacteristic condition. *Mathematical Models and Methods in Applied Sciences*, 21(12):2379–2407, 2011.
- [6] K. E. T. Giljarhus, S. T. Munkejord, and G. Skaugen. Solution of the Span–Wagner equation of state using a density–energy state function for fluid-dynamic simulation of carbon dioxide. *Industrial & Engineering Chemistry Research*, 51(2):1006–1014, 2011.
- [7] M. Hammer, Å. Ervik, and S. T. Munkejord. Method using a density–energy state function with a reference equation of state for fluid-dynamics simulation of vapor–liquid–solid carbon dioxide. *Industrial & Engineering Chemistry Research*, 52(29):9965–9978, 2013.
- [8] R. S. Haszeldine. Carbon capture and storage: How green can black be? *Science*, 325(5948):1647–1652, 2009.
- [9] *Technology Roadmap: Carbon capture and storage*. IEA, 2013.
- [10] *Energy Technology Perspectives*. IEA, 2015.
- [11] D. I. Ketcheson and A. C. Robinson. On the practical importance of the SSP property for Runge–Kutta time integrators for some common Godunov-type schemes. *International Journal for Numerical Methods in Fluids*, 48(3):271–303, 2005.

- [12] K. Kitamura, M. S. Liou, and C. H. Chang. Extension and comparative study of ausm-family schemes for compressible multiphase flow simulations. *Communications in Computational Physics*, 16(3):632–674, September 2014.
- [13] B. Leonard. Comparison of truncation error of finite-difference and finite-volume formulations of convection terms. *Applied Mathematical Modelling*, 18(1):46 – 50, 1994.
- [14] R. J. LeVeque. *Numerical methods for conservation laws*, volume 132. Springer, 1992.
- [15] R. J. LeVeque. *Finite volume methods for hyperbolic problems*, volume 31. Cambridge university press, 2002.
- [16] M. S. Liou. A sequel to AUSM, AUSM+. *Journal of Computational Physics*, 129:364–382, 1996.
- [17] M. S. Liou. A sequel to AUSM, part II: AUSM+-up for all speeds. *Journal of Computational Physics*, 214:137–170, 2006.
- [18] M. S. Liou and C. J. Steffen. A new flux splitting scheme. *Journal of Computational physics*, 107:23–39, 1993.
- [19] M.-S. Liou. The evolution of AUSM schemes. *Defence Science Journal*, 60(6):606–613, 2010.
- [20] M. J. Mølnevik, G. Tangen, R. Aarlien, and N. A. Røkke. BIGCCS centre–boosting CCS research and innovation. *Energy Procedia*, 4:6133–6140, 2011.
- [21] B. Müller. Introduction to computational fluid dynamics (unpublished). Department of Energy and Process Engineering, Norwegian University of Science and Technology (NTNU), 2014.
- [22] S. T. Munkejord and M. Hammer. Depressurization of CO₂-rich mixtures in pipes: Two-phase flow modelling and comparison with experiments. *International Journal of Greenhouse Gas Control*, 37:398–411, 2015.
- [23] S. T. Munkejord, S. Evje, and T. Flåtten. A MUSTA cheme for a nonconservative two-fluid model. *SIAM Journal on Scientific Computing*, 31(4):2587–2622, 2009.
- [24] H. Paillère, C. Corre, and J. R. García Cascales. On the extension of the AUSM+ scheme to compressible two-fluid models. *Computers & Fluids*, 32(6):891–916, 2003.
- [25] R. H. Pletcher, J. C. Tannehill, and D. Anderson. *Computational fluid mechanics and heat transfer*. CRC Press, 2012.
- [26] J. S. Sachdev, A. Hosangadi, and V. Sankaran. Improved flux formulations for unsteady low mach number flows. In *AIAA Paper No. 2012-3067, 42nd AIAA Fluid Dynamics Conference*, 2012.
- [27] V. Scott, S. Gilfillan, N. Markusson, H. Chalmers, and R. S. Haszeldine. Last chance for carbon capture and storage. *Nature Climate Change*, 3(2):105–111, 2013.

-
- [28] E. Shima and K. Kitamura. On AUSM-family scheme for all speeds with shock detection for carbuncle-fix. *AIAA-Paper*, 3544:2009, 2009.
- [29] C.-W. Shu. A survey of strong stability preserving high order time discretizations. *Collected lectures on the preservation of stability under discretization*, 109:51–65, 2002.
- [30] R. Span and W. Wagner. A new equation of state for carbon dioxide covering the fluid region from the triple-point temperature to 1100 K at pressures up to 800 MPa. *Journal of Physical and Chemical Reference Data*, 25(6):1509–1596, 1996.
- [31] V. Titarev and E. Toro. Musta schemes for multi-dimensional hyperbolic systems: analysis and improvements. *International journal for numerical methods in fluids*, 49(2):117–148, 2005.
- [32] E. F. Toro. *Riemann Solvers and Numerical Methods for Fluid Dynamics: A Practical Introduction*. Springer, 2009. ISBN 978-3-540-49834-6.
- [33] E. F. Toro. Musta: A multi-stage numerical flux. *Applied Numerical Mathematics*, 56(10):1464–1479, 2006.
- [34] B. Van Leer. Towards the ultimate conservative difference scheme. V. A second-order sequel to Godunov’s method. *Journal of Computational Physics*, 32(1):101–136, 1979.